Volume: 4 Issue: 2 2023

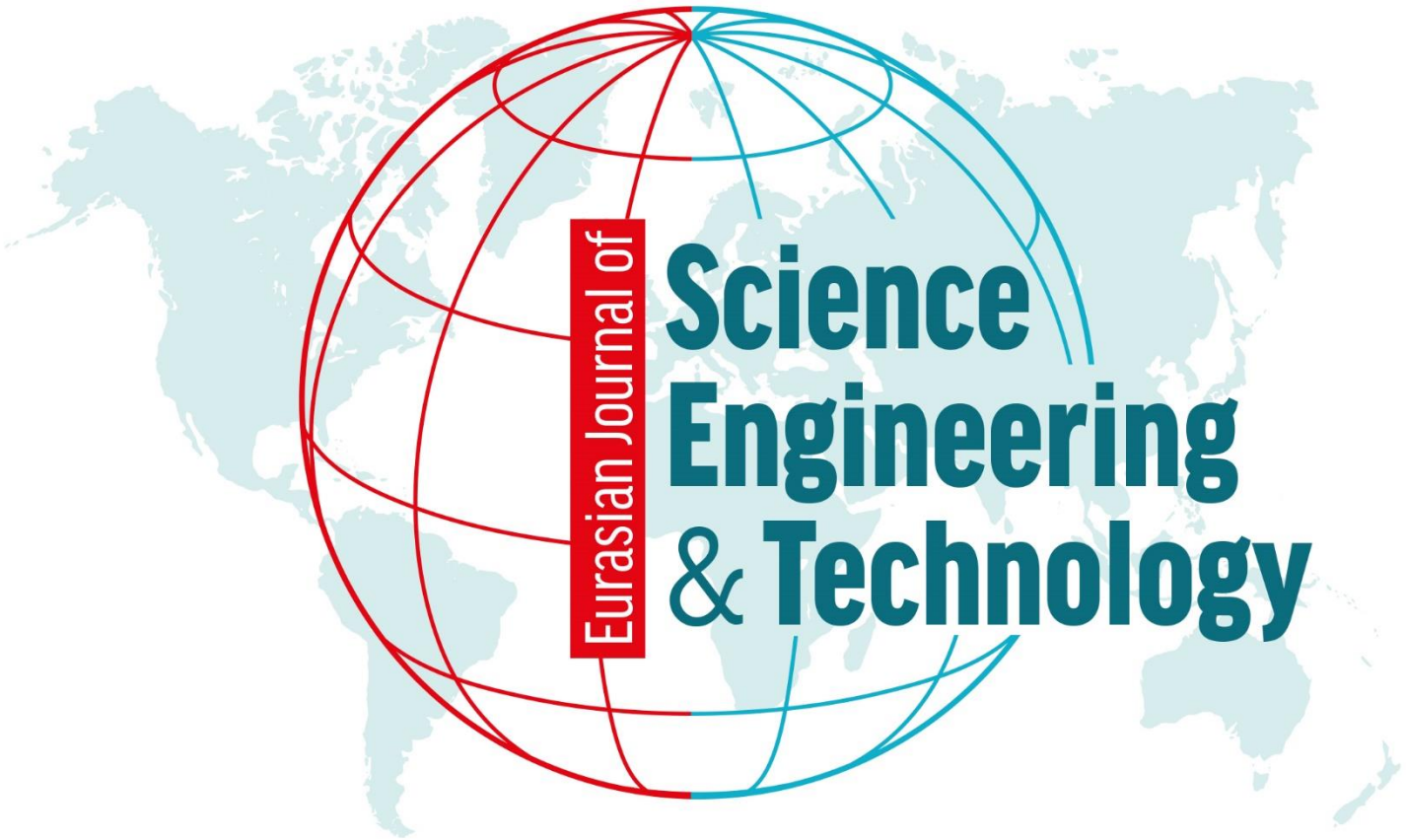

Eurasian Journal of Science Engineering and Technology

Editors

Editorial Board

Eurasian Journal of Science Engineering and Technology

Scientific Board

Eurasian Journal of Science Engineering and Technology

Correspondence Address

Niğde Ömer Halisdemir University
Eurasian Journal of Science Engineering and Technology Publishing Coordinatorship, 51240
Niğde/Türkiye

***E-mail*:** recep.zan@ohu.edu.tr
mbarut@ohu.edu.tr

***Web page*:** https://dergipark.org.tr/tr/pub/ejset

Publication information

The objective of Eurasian Journal of Science Engineering and Technology (EJSET) is to provide an academic environment for researchers in various fields of science and engineering and for the publication and dissemination of high-quality research results in the fields of science, applied science, engineering, architecture, agricultural science and technology.

Eurasian Journal of Science Engineering and Technology

CONTENTS/*İÇİNDEKİLER*

Eurasian Journal of Science Engineering and Technology

Research Article

EXPLORING EFFICIENCY AND DESIGN OPTIMIZATION OF FLEXIBLE PEROVSKITE SOLAR CELLS USING SCAPS-1D SIMULATION

Elif DAMGACI[1*], Emre KARTAL[2], Ayşe SEYHAN[3]

[1,2,3] *Nigde Omer Halisdemir University, Nanotechnology Research Center, 51240, Nigde, Türkiye*
[1] *Nigde Omer Halisdemir University, Department of Mechanical Engineering, 51240, Nigde, Türkiye*
[2,3] *Nigde Omer Halisdemir University, Department of Physics, 51240, Nigde, Türkiye*

ABSTRACT

This research focuses on using SCAPS-1D software to design and simulate efficient flexible perovskite solar cells. The study aims to optimize design parameters, gain a deeper understanding of the underlying physics, and obtain valuable insights into electrical characteristics. The device architecture includes key components like PET/ITO substrate, TiO_2 ETL, $CH_3NH_3SnI_3$ absorber, CuSCN HTL, and Au electrode. By optimizing the absorber thickness (600 nm) and temperature (300 K), the performance and efficiency of the cell were improved. Investigation of different doping concentrations at 300 K for a fixed thickness revealed an efficiency of 26.98% at 600 nm. The highest efficiency of 31.44% was achieved with a doping concentration of 1E+21. This research showcases the potential of flexible perovskite solar cells for lightweight and versatile applications, emphasizing their significance in the field.

Keywords: Flexible perovskite solar cells, SCAPS-1D, Simulation, Doping, Efficiency.

1. INTRODUCTION

The advent of flexible perovskite solar cells has brought about a promising technology in the realm of photovoltaics. These devices exhibit remarkable power conversion efficiency and possess the unique ability to conform to diverse surfaces. In comparison to traditional rigid solar cells, flexible perovskite solar cells (FPSCs) offer substantial advantages, including their lightweight nature and bendable characteristics. These attributes enable their application in areas where conventional solar cells are impractical or constrained by their rigidity.

The efficiency of FPSCs demonstrated remarkable progress, experiencing a substantial increase from 2.6% to 19.5% over the period of 2013 to 2019. This significant improvement in productivity highlights the rapid advancements in FPSC technology during that timeframe [1,2]. Presently, single-junction FPSCs have achieved power conversion efficiencies (PCEs) of 21.76%. In comparison, tandem-inverted FPSCs have achieved even higher PCEs of 24.7%. These significant efficiency values underscore the promising commercial potential of both single-junction and tandem-inverted FPSCs [3]. The optical and electrical properties of flexible substrate perovskite solar cells produced in different structures with high efficiency over time are given in Table 1.

Table 1. 2013-2023 Flexible perovskite cell efficiency values.

Configuration	Voc	FF	Jsc	PCE	Ref	Year
PET/ITO/PEDOT:PSS/Perovskite/PCBM/TiO_x/Al	0.88	51	14.4	6.4	[4]	2013
PEN/ITO/ $MAPbI_{3-x}Cl_x$/Spiro-OMeTAD/Ag	0.95	60	21.40	12.20	[5]	2014
PEN/ITO/ZnO/$MAPbI_3$/PTAA/Au	1.10	75	18.7	15.4	[6]	2015
PET/ITO/ZnO/$MAPbI_3$/PTAA/Au	1.10	79	19.3	16.8	[7]	2018
PEN/ITO/SnO_2/Perovskite/Spiro-OMeTAD/Au	1.08	74.9	21.3	17.3	[8]	2019
PEN/ITO/SnO_2-CPTA/Perovskite/Spiro-OMeTAD /Au	1.08	75.0	22.4	18.3	[9]	2019
PET/ITO/SnO_2 NPs/$(FAPbI_3)0.95(MAPbBr_3)0.05$/ spiro-OMeTAD/Au	1.14	75.5	22.1	19.1	[10]	2020
PET/PEDOT:PSS/PTAA/Perovskite/PCBM/BCP/Ag	-	-	-	21.02	[11]	2022
PEN/ITO/SAM/PVK/PCBM/BCP/Ag	1.178	83.55	23.36	23.01	[12]	2023

* Corresponding author, e-mail: elifdamgaci@gmail.com (E. Damgacı)
Recieved: 26.05.2023 Accepted: 16.06.2023
doi: 10.55696/ejset.1303146

The experimental investigation and characterization of the layers comprising the cell structure have been extensively conducted by numerous researchers, as presented in Table 1. The SCAPS software is utilized to simulate and analyze the performance characteristics of the FPSC device, allowing for the optimization and understanding of its electrical behavior. Using the SCAPS software, a detailed understanding of the device's performance has been gained, contributing to the optimization and advancement of flexible perovskite solar cell technology. Based on these research studies, the simulation program enables the calculation of the cell's efficiency, occupancy factor, current, and voltage values.

2. MATERIAL AND METHOD

SCAPS 1D (Solar Cell Capacitance Simulator) is a powerful software tool widely utilized in the field of solar cell research and development. Its primary function is to simulate and model the intricate electrical behavior exhibited by solar cells. This sophisticated tool enables scientists, engineers, and researchers to delve into the intricacies of solar cell operation, ultimately leading to a better understanding of their performance and aiding in the optimization of various solar cell devices.

The basic equations used in SCAPS programming are:

$$\vec{\nabla}.\varepsilon\vec{\nabla}\varphi = -q(p - n + ND + -NA -) \quad (1)$$

$$Jn = Dn\frac{dn}{dx} + \mu_n n\frac{d\emptyset}{dx},\ Jp = Dp\frac{dp}{dx} + \mu_p p\frac{d\emptyset}{dx} \quad (2)$$

$$\frac{dj_n}{dx} = G - R,\ \frac{dj_P}{dx} = G - R \quad (3)$$

The current study presents a model and simulation of a typical PSC with five layers, including a conductive Gold (Au) metal electrode, TiO_2 as the electron transport material (ETM) layer, methylammonium tin tri-iodide ($CH_3NH_3SnI_3$) as the perovskite light absorber layer, Copper (I) thiocyanate (CuSCN) as the hole transport material (HTM) layer, and Indium Tin Oxide (ITO)-coated flexible polyethylene terephthalate (PET) as the substrate. The simulated structure and energy band diagram are given in Figure 1(a) and Figure 1. (b).

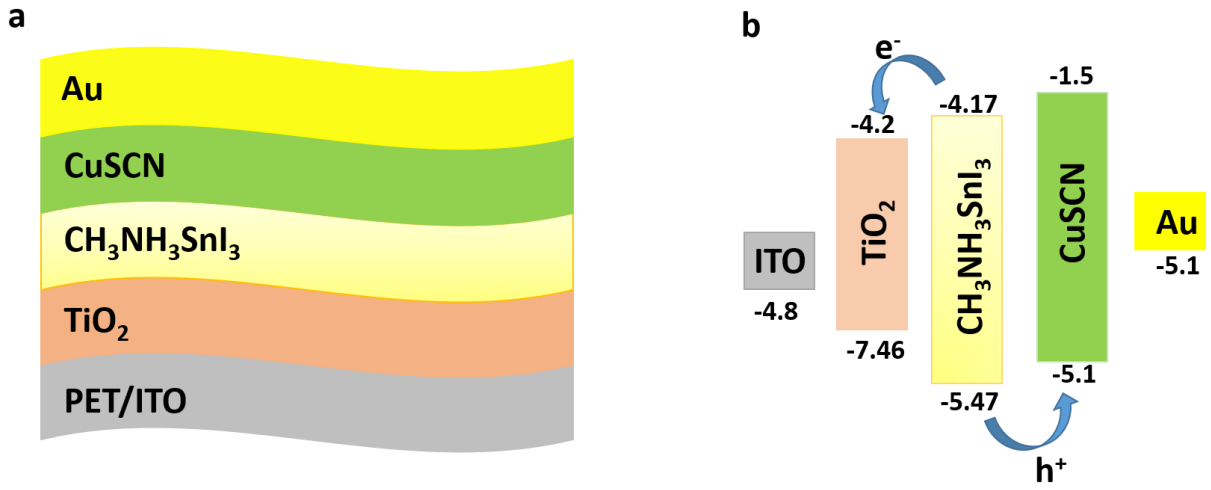

Figure 1. Flexible perovskite solar cell structure (a), the energy band diagram (b).

Burgelman et al. developed and adapted the SCAPS 1D program for the purpose of designing and conducting numerical analysis on the cell architecture of solar cells. The program also enables simulation and numerical analysis of optoelectronic and photovoltaic architectures, providing valuable insights for research in these fields. SCAPS 1D is capable of modeling and analyzing the recombination mechanism, electric field distribution, charge transport, and current densities of various types of

solar cells. It can solve the basic semiconductor equations in one dimension at a steady state, making it suitable for describing the model of any solar cell.

In this study, the most up-to-date version of the program, SCAPS 1D (ver.3.3.10), was used by simulating the device efficiency parameters closest to the literature values. The operation of the program is given in the following steps and the interface shape is shown in Figure 2. SCAPS 1D is a software tool used for simulating and analyzing the performance of photovoltaic devices. Here are the working steps to use SCAPS 1D:

1. Start SCAPS 1D: Launch the SCAPS 1D software on your computer.
2. Set the desired problem: Define the specific problem you want to simulate. This could be the analysis of a specific solar cell structure, material, or device configuration.
3. Input photovoltaic parameters: Provide the necessary input parameters for the simulation. These parameters include material properties, device geometries, doping profiles, and other relevant information specific to the problem you are investigating.
4. Apply the working condition: Specify the working conditions under which you want to analyze the photovoltaic device. This includes setting parameters such as temperature, light intensity, and applied voltages or currents.
5. Run the problem: Initiate the simulation by running the problem within the SCAPS 1D software. The software will use the input parameters and working conditions to calculate the behavior of the photovoltaic device.
6. Analyze the output: After the simulation is complete, SCAPS 1D will provide output data and results. This may include information such as current-voltage characteristics, efficiency, charge carrier distribution, and other relevant performance metrics.

By following these steps, you can utilize SCAPS 1D to simulate and study the behavior of photovoltaic devices under different conditions and configurations [13].

Table 2 presents the essential cell parameters necessary for the simulation, emphasizing their significance. The selection of these values was based on a combination of theoretical analysis, experimental findings, and references from established literature. In certain instances, reasonable approximations were made when data was unavailable [14,15,16]. The majority of absorber layer parameters employed in the simulation were obtained from relevant literature sources.

Table 2. Materials parameters of various layers simulated for flexible perovskite solar cells at A.M. 1.5G.

Parameter	ITO	TiO_2	$CH_3NH_3SnI_3$	CuSCN
Thickness (nm)	300	100	Varied	50
Bandgap (eV)	3.65	3.26	1.3	3.6
Electron affinity (eV)	4.8	4.2	4.17	1.7
Permittivity (ε)	8.900	10	6500	10000
CB effective DOS (cm^{-3})	5.200E+18	2.2E+18	1.0E+18	2.200E+19
VB effective DOS (cm^{-3})	1000E+18	1.800E+19	1.000E+19	1.800E+19
Electron thermal Velocity (cm/s)	2000E+7	1.000E+7	1.000E+7	1.000E+7
Hole thermal Velocity (cm/s)	1000E+7	1.000E+7	1.000E+7	1.000E+7
Electron mobility, μ_E (cm^2/Vs)	1000E+1	1.000E+2	1.600E+0	2.500E-1
Hole mobility, μ_H (cm^2/Vs)	1000E+1	2.500E+1	1.600E+0	2.500E-1
Donor density ND ($1/cm^3$)	1000E+20	1.000E+19	0.00E+0	0.00E+0
Acceptor density NA ($1/cm^3$)	1000E+15	0.00E+0	Varied	2.000E+19

Table 3. The basic material parameters of the back and front contacts for cell.

Electrical properties @ 300 K	BC (Au)	FC(PET/ITO)
Thermionic emission/surface recombination velocity of electron(cm/s)	10^5	10^7
Thermionic emission/surface recombination velocity of hole(cm/s)	10^7	10^5
Work function(eV)	5.1[17]	4.7[18]

***BC:Back contact, FC:Front contact**

The software interfaces incorporate all the variables listed in Table 2 and Table 3, which serve as input parameters for the device simulation. This ensures that the simulation accurately reflects the behavior of the physical device. Moreover, it provides a comprehensive list of the parameters considered throughout the procedure, enabling the exploration of different elements' effects on device performance by manipulating variables. Figure 2 below illustrates the detailed simulation procedure. This program, which can be applied to various solar cells, is updated with different materials and photovoltaic parameters.

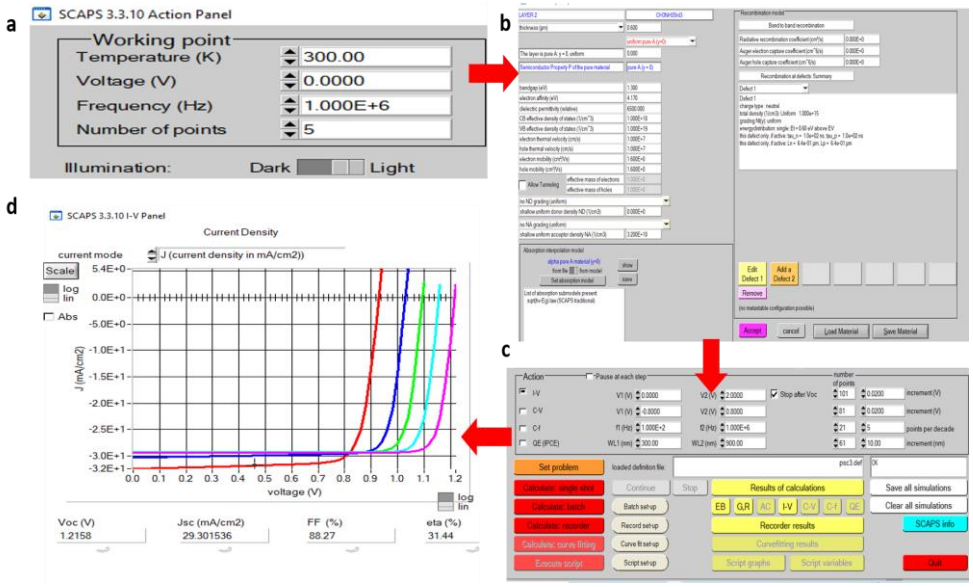

Figure 2. The SCAPS 1D working point (a), setting problem and Input Photovoltaic Parameters (b), batch calculation and record calculation (c), J-V results (d).

3. RESULTS AND DISCUSSION

Overall, understanding and addressing the impact of temperature on flexible perovskite solar cells are crucial for optimizing their performance, stability, and long-term reliability, thereby facilitating their widespread adoption as a renewable energy technology. High temperatures have a detrimental impact on the power conversion efficiency of flexible perovskite solar cells. The underlying cause is the accelerated occurrence of non-radiative recombination processes within the perovskite layer. This elevated recombination rate leads to a drop in both the open circuit voltage and the fill factor, resulting in an overall drop in efficiency. These effects can be observed in figures generated using SCAPS 1D simulations. Table 4 shows detailed simulation data of simulated flexible photovoltaic cells (FPCs) on filling factor (FF), open circuit voltage (Voc), FF, short circuit current density (Jsc), and variable temperature effect on PCE. In Table 5, Simulated FPCs were investigated with varying thicknesses to examine their effects on FF, Voc, Jsc, and PCE. Due to the deformation and increased stress resulting from temperature elevation, the layers within the simulated model may experience enhanced interconnectivity. PET/ITO melting temperature ranges from 120 degrees to 260 degrees. This percentage has been optimized considering the temperature value in the simulation. This can lead to a decrease in fill factor and efficiency, as the rise in series resistance coincides with a reduction in diffusion length [19].

To achieve high efficiency, the optimum temperature for the simulated model was determined to be 300 K, as depicted in figure 3. Furthermore, the thickness optimization procedures were conducted at this temperature.

Table 4. Varies temperature effect on Voc, FF, Jsc, and PCE of the simulated FPSC.

Temperature (K)	Voc	FF	Jsc	Eta%
250	1.1159	79.93	28.69585	25.60
298.15	1.0657	85.63	29.553916	26.97
300	1.0636	85.74	29.579213	26.98
350	1.0078	85.81	30.127254	26.06
400	0.9502	84.11	30.508975	24.38
450	0.8906	82.11	30.803791	22.53
500	0.8292	79.80	31.035678	20.54

Table 5. Varies thickness effect on Voc, FF, Jsc, and PCE of the simulated FPSC at 300 K.

Thickness (nm)	Voc	FF	Jsc	Eta%
400	1.0681	86.16	28.827141	26.53
500	1.0656	86.00	29.411375	26.95
600	1.0636	85.74	29.579213	26.98
700	1.0620	85.66	29.560310	26.89
800	1.0607	85.60	29.467137	26.76
900	1.0598	85.56	29.353818	26.62
1000	1.0591	85.53	29.244978	26.49

The performance of solar cells is influenced by the thickness of the absorber layer (L). Figure 3 demonstrates how varying the absorber layer thickness impacts performance parameters such as Voc, Jsc, FF, and PCE. In the cells that underwent thickness optimization, the highest efficiency value of 26.98% was achieved at a thickness of 600 nm.

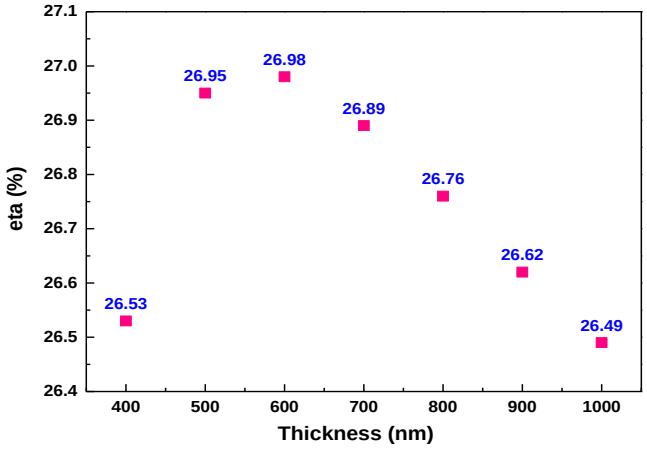

Figure 3. The effect of $CH_3NH_3SnI_3$ layer thickness on efficiency.

In the SCAPS 1D simulation, the acceptor density (NA) is an important parameter that is considered to accurately model the behavior of the device. The concentration of doping within the absorber material significantly impacts the performance of photovoltaic systems. The study examines the performance of a proposed flexible perovskite solar cell by investigating its response to different doping densities in the absorber layer. Figure 4 displays the variations of Voc, Jsc, FF, and overall efficiency of the designed perovskite solar cell as a function of the doping concentration in the absorber layer.

EXPLORING EFFICIENCY AND DESIGN OPTIMIZATION OF FLEXIBLE PEROVSKITE SOLAR CELLS USING SCAPS-1D SIMULATION

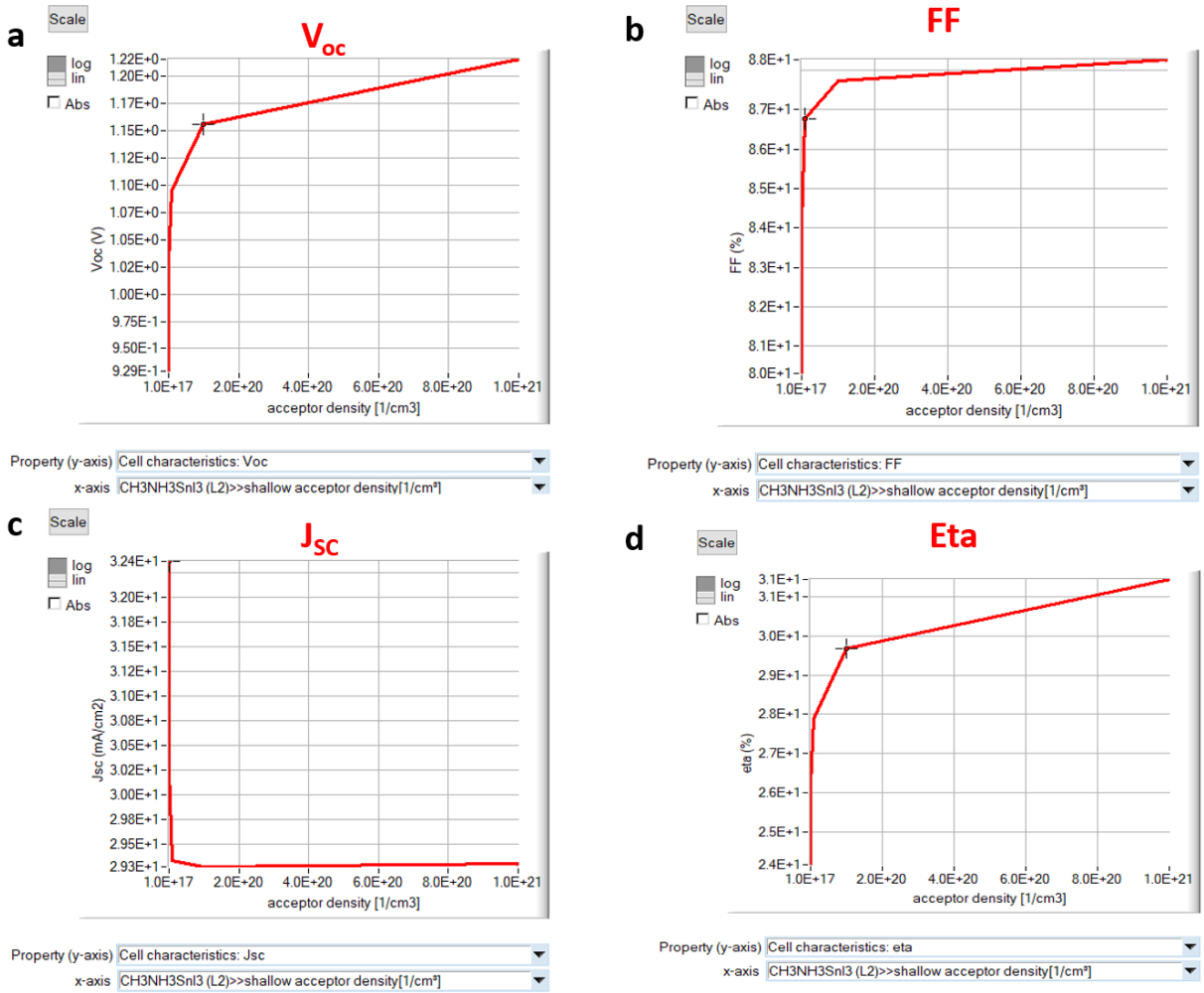

Figure 4. The effect of NA of the $CH_3NH_3SnI_3$ absorber layer on the performance of (a) Voc, (b) FF (c) Jsc, and (d) PCE.

Shallow uniform acceptor density NA ($1/cm^3$) effect on V_{oc}, J_{sc}, FF, and efficiency is as follows; firstly, the acceptor doping concentration affects the energy levels and recombination processes in the perovskite layer. An optimal NA can create an appropriate energy gradient, reducing recombination and enhancing the Voc. Secondly, the acceptor doping concentration also influences the charge carrier transport and recombination within the perovskite layer. An optimized NA can enhance charge carrier mobility, minimize recombination losses, and improve the FF. When a solar cell operates at a higher fill factor, it typically operates closer to its maximum power point, which corresponds to the optimal balance between voltage and current. By operating at higher currents and voltages closer to the maximum power point, the overall power conversion efficiency of the solar cell increases. This, in turn, means that a higher fraction of the incident light is being effectively converted into usable electrical power, reducing the potential for parasitic absorption. Thirdly, the acceptor doping concentration indirectly affects the Jsc by influencing the charge carrier generation and transport. In some cases, an appropriate NA can enhance the Jsc by optimizing the charge carrier extraction and reducing recombination. However, if NA is excessively high, it can increase trap-assisted recombination and hinder the charge carrier generation, leading to a decrease in Jsc. Therefore, it is important to carefully select the acceptor doping concentration in the perovskite layer to achieve higher Voc, FF, and Jsc, striking a balance between optimizing charge carrier transport and minimizing recombination losses. In this study, simulating the doping concentration in the range of $1x10^{17}$ to $1x10^{21}$, it was observed that the Voc and FF increased, while the Jsc decreased. This suggests that there is an optimal doping concentration within this range that enhances Voc and FF but compromises Jsc. It indicates a trade-off between improving Voc and FF while potentially sacrificing Jsc in the context of the specific doping concentrations studied [20].

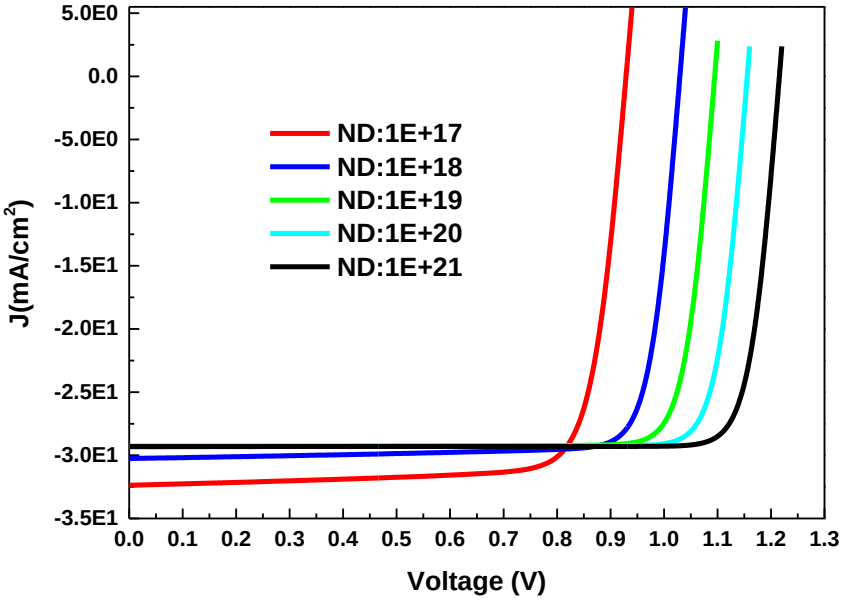

Figure 5. Acceptor density NA (1/cm^3) effect on PCE.

Table 6. Varies acceptor density effect on Voc, FF, Jsc, and PCE of the simulated FPSC at 300 K and 600 nm thickness.

Density NA (1/cm^3)	Voc	J_{SC}	FF	Eta%
1E+17	0.9292	32.369757	80.31	24.15
1E+18	1.0299	30.252599	84.09	26.20
1E+19	1.0949	29.338074	86.78	27.87
1E+20	1.1558	29.271885	87.72	29.68
1E+21	1.2185	29.301536	88.07	31.44

Table 6 presents the optical values for flexible perovskite solar cells, organized based on the doping concentration ratios.The optimization of thickness was performed on a flexible perovskite solar cell at 300 K. As seen in figure 5 with doping concentrations of 1E+17, 1E+18, 1E+19, 1E+20, and 1E+21, a thickness of 600 nm resulted in an efficiency value of 26.98%. Among these doping concentrations, the highest efficiency of 31.44% was achieved with a doping concentration of 1E+21.

4. CONCLUSION

In this study, a simulation-based analysis was conducted on PET/ITO/TiO_2/$CH_3NH_3SnI_3$ /CuSCN/Ag flexible perovskite solar cells. The purpose of the analysis was to investigate the performance and characteristics of these specific solar cell configurations by using SCAPS 1D. In the optimization study of a flexible perovskite solar cell at 300 K, different doping concentrations were investigated for a fixed thickness of 600 nm. The resulting efficiency values showed that at this thickness, the cell achieved an efficiency of 26.98%. Among the tested doping concentrations, the highest efficiency of 31.44% was obtained with a doping concentration of 1E+21.

SIMILARITY RATE: 15 %

CONFLICT of INTEREST

The authors declared that they have no known conflict of interest.

ACKNOWLEDGEMENT

The authors gratefully acknowledge Professor Marc Burgelman from the Department of Electronics and Information Systems at the University of Ghent for the development of the SCAPS software package and for granting permission to utilize it in this study.

REFERENCES

[1] Kumar, Mulmudi Hemant, et al. "Flexible, low-temperature, solution processed ZnO-based perovskite solid state solar cells." *Chemical Communications* 49.94 (2013): 11089-11091.
[2] Huang, Keqing, et al. "High-performance flexible perovskite solar cells via precise control of electron transport layer." *Advanced Energy Materials* 9.44 (2019): 1901419.
[3] Xu, Zhiyuan, et al. "Functional layers of inverted flexible perovskite solar cells and effective technologies for device commercialization." *Small Structures* (2023): 2200338.
[4] Docampo, Pablo, et al. "Efficient organometal trihalide perovskite planar-heterojunction solar cells on flexible polymer substrates." *Nature Communications* 4.1 (2013): 2761.
[5] Di Giacomo, Francesco, et al. "Flexible perovskite photovoltaic modules and solar cells based on atomic layer deposited compact layers and UV-irradiated TiO2 scaffolds on plastic substrates." *Advanced Energy Materials* 5.8 (2015): 1401808.
[6] Heo, Jin Hyuck, et al. "Highly efficient low temperature solution processable planar type CH3NH3PbI3 perovskite flexible solar cells." *Journal of Materials Chemistry A* 4.5 (2016): 1572-1578.
[7] Lee, Eunsong, et al. "All-Solution-Processed Silver Nanowire Window Electrode-Based Flexible Perovskite Solar Cells Enabled with Amorphous Metal Oxide Protection." *Advanced Energy Materials* 8.9 (2018): 1702182.
[8] Liu, Chang, et al. "Hydrothermally treated SnO2 as the electron transport layer in high-efficiency flexible perovskite solar cells with a certificated efficiency of 17.3%." *Advanced Functional Materials* 29.47 (2019): 1807604.
[9] Zhong, Meiyan, et al. "Highly efficient flexible MAPbI 3 solar cells with a fullerene derivative-modified SnO2 layer as the electron transport layer." *Journal of Materials Chemistry A* 7.12 (2019): 6659-6664.
[10] Qi, Jiabin, et al. "A kirigami-inspired island-chain design for wearable moistureproof perovskite solar cells with high stretchability and performance stability." *Nanoscale* 12.6 (2020): 3646-3656.
[11] Cheng, Haiyang, et al. "KBF4 Additive for Alleviating Microstrain, Improving Crystallinity, and Passivating Defects in Inverted Perovskite Solar Cells." *Advanced Functional Materials* 32.36 (2022): 2204880.
[12] Han, Bin, et al. "Rational Design of Ferroelectric 2D Perovskite for Improving the Efficiency of Flexible Perovskite Solar Cells Over 23%." *Angewandte Chemie International Edition* 62.8 (2023): e202217526.
[13] Marc. Burgelman, Department of Electronics and Information System, University of Gent. SCAPS-1D.
[14] Anwar, Farhana, et al. "Effect of different HTM layers and electrical parameters on ZnO nanorod-based lead-free perovskite solar cell for high-efficiency performance." *International Journal of Photoenergy* 2017 (2017).
[15] Hossain, M. Khalid, et al. "Effect of various electron and hole transport layers on the performance of CsPbI3-based perovskite solar cells: A numerical investigation in DFT, SCAPS-1D, and wxAMPS frameworks." *ACS omega* 7.47 (2022): 43210-43230.
[16] Hossain, M. Khalid, et al. "An extensive study on multiple ETL and HTL layers to design and simulation of high-performance lead-free CsSnCl3-based perovskite solar cells." *Scientific Reports* 13.1 (2023): 2521.
[17] Behrouznejad, Fatemeh, et al. "A study on utilizing different metals as the back contact of CH3NH3PbI 3 perovskite solar cells." *Journal of Materials chemistry A* 4.35 (2016): 13488-13498.
[18] Goje, A. A., et al. "Design and Simulation of Lead-free Flexible Perovskite Solar cell Using SCAPS-1D." *IOP Conference Series: Materials Science and Engineering*. Vol. 1278. No. 1. IOP Publishing, 2023.
[19] Slami, Abdelhadi, Mama Bouchaour, and Laarej Merad. "Numerical study of based perovskite solar cells by SCAPS-1D." *Int. J. Energy Environ* 3 (2019): 17-21.
[20] Trukhanov, V. A., V. V. Bruevich, and D. Yu Paraschuk. "Effect of doping on performance of organic solar cells." *Physical Review B* 84.20 (2011): 205318.

Eurasian Journal of Science Engineering and Technology

Research

THE EXOGAM2 CALIBRATION USING THE NEWLY DEVELOPED NUMEXO2 DIGITAL ELECTRONIC

Elif ŞAHİN [1,*], Sefa ERTÜRK[2], Vakkas BOZKURT[3]

[1] *Institut für Kernphysik, Technische Universität Darmstadt, D-64289 Darmstadt, Germany*
[1]*GSI Helmholtzzentrum für Schwerionenforschung, 64291 Darmstadt, Germany*
[2]*Niğde Ömer Halisdemir University, Faculty of Medicine, Department of Biophysics, 51240 Niğde, Türkiye*
[3] *Niğde Ömer Halisdemir University, Department of Physics, 51240 Niğde, Türkiye*

ABSTRACT

In this study, the calibration process of the EXOGAM2 conventional gamma detector system with the newly developed digital electronic device, namely NUMEXO2, will be presented. This experimental study was performed at the GANIL (Grand Accélérateur National d'Ions Lourds) nuclear research center in France. The energy calibration of the EXOGAM2 detector system with the newly developed NUMEXO2 digital electronic device was conducted using both low and high gamma energy levels of a ^{152}Eu radioactive source. This calibration was carried out for two EXOGAM2 detectors, and the energy resolution of each crystal in the EXOGAM2 system was determined.

The energy resolution of each crystal was found to be reasonable energy resolution values of the EXOGAM2 detectors. Therefore, the use of the digital electronic device NUMEXO2 did not affect the energy resolution of the detectors, but it did enable us to acquire data at a high counting rate.

Keywords: EXOGAM2, NUMEXO2, Digital electronic, Calibration

1. INTRODUCTION

The aim of this study is to demonstrate the design, performance verification and efficiency of a digital electronic system, namely NUMEXO2, with an EXOGAM2 (EXOtic GAMma array) detector located at GANIL, France [1,2]. Gamma-ray spectroscopy is the most widely used technique for observing nuclear characteristics, providing insights into the behavior and structure of nuclei.

A detector system can be used to distinguish a new radioisotope by analyzing the properties of the gamma rays spectrum and determining the levels of gamma energy. Over the past year, significant advancements have been made in detector systems through the integration of novel technologies. As a result, the conventional analog electronics of these systems have been replaced with digital electronics. There are several reasons behind this transition to digital electronics, including the ability to handle high counting rates, facilitate complex data sets, and improve overall performance without compromising the energy resolution of the detectors.

Nuclear structural physics is currently focused on revealing the properties of new exotic nuclei. Previously very competent devices such as high purity germanium (HP-Ge) systems EUROBALL [3], GAMMASPHERE [4], MINIBALL [5], and EXOGAM [4] were commonly used. In recent years, AGATA [6], GRETINA [7], JUROGAM II [8], and EXOGAM2 [2], coupled with the newly developed digital electronic system NUMEXO2, have been employed to detect of gamma rays emitted from nuclear reactions. In addition, the Neutron Shell and Neutron Wall used to use as neutron detectors [9, 10, 11], while the newer arrays are coupled with the NEDA [12,13] neutron detector array and ancillary charged particle detector arrays such as DIAMANT [14]. Both NEDA and DIAMANT also utilize the digital electronic system NUMEXO2.

Semiconductor types of Germanium (Ge) detectors were developed in the 1970s and 1980s, focusing on volume and purity [15–17]. Significant advancements in highly segmented Ge detectors have greatly improved their efficiency and energy resolution. The capacity to categorize between two gamma rays with closely spaced energies necessitates high energy resolution detectors. As a result, HPGe detectors such as AGATA, GRETINA, and EXOGAM2 are renowned for their superior energy resolution. Achieving excellent energy resolution relies on both the electronics and type of detector. Energy resolution is usually determined using a metric known as full width at half maximum (FWHM), which quantifies the distribution at half width of the peak.

Figure 1 shows the peak or pulse shape, the energy resolution is described by the formula FWHM=2.35σ, where σ represents the standard deviation of the Gaussian shape. The lower the FWHM value, the higher the sensitivity level of the detector, allowing the separation of closely related gamma energies..

* Corresponding author, e-mail: ecelifsahin@gmail.com
Recieved: 11.06.2023 Accepted: 20.11.2023
doi: 10.55696/ejset.1312972

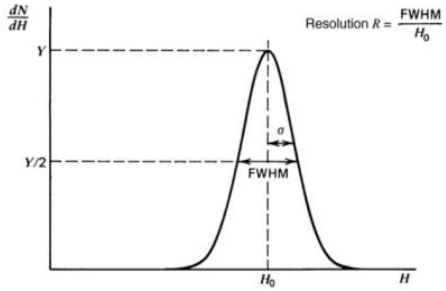

Figure 1. Detector response function in Gaussian form.

The main objective of the EXOGAM design was to optimize the efficiency of the light peaks, in other words to maximize the total efficiency of the light peaks while maintaining the quality of the spectra. Searching for new exotic nuclei also requires experiments with exotic beams, which is a highly challenging process to achieve a high signal-to-noise ratio and good resolution [18]. Instead of an analog system a digital electronic system should be used, resulting in the production of a new digital electronic system for EXOGAM, from now on referred to as EXOGAM2.

EXOGAM2 comprises an array of high-resolution germanium detectors positioned in close proximity to the target point. These detectors have been strategically organized to achieve a high photo-peak efficiency of 20% at 1.3 MeV gamma rays [19]. Each germanium detector is surrounded by an escape suppression shield typically made of bismuth germanate (BGO).

This suppression shield enhances the quality of the spectrum. The high-purity germanium detectors used in EXOGAM are coaxial n-type HPGe crystals. Additionally, each of the four germanium crystals constitutes a segmented CLOVER detector placed within the same cryostat.

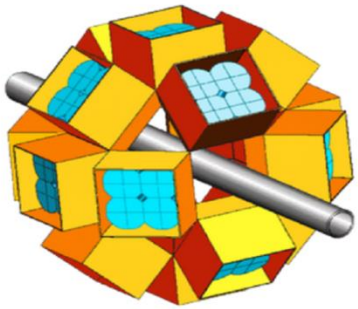

Figure 2. EXOGAM detector array design [2].

2. MATERIAL AND METHOD

CLOVER detectors that have been segmented make up the EXOGAM2 design. Electronic segmentation has separated each Germanium crystal into four areas and placed them all in the same cryostat (Figure 3). This segmentation is a crucial requirement in order to have a large volume and to more accurately pinpoint the gamma ray impact point in the detector. Additionally, the segmentation design's closed-packed and effective construction aid in reducing Doppler broadening. A high level of granularity is required to maintain reasonable resolution and accommodate the Doppler broadening of the gamma-ray peaks [20]. Segmentation is consequently used to achieve granularity. In the Clover detector, each Germanium crystal includes an interior contact and four exterior contacts that are situated at each crystal's corners. These contacts make it possible to describe the location of the event (right side in Figure 3)

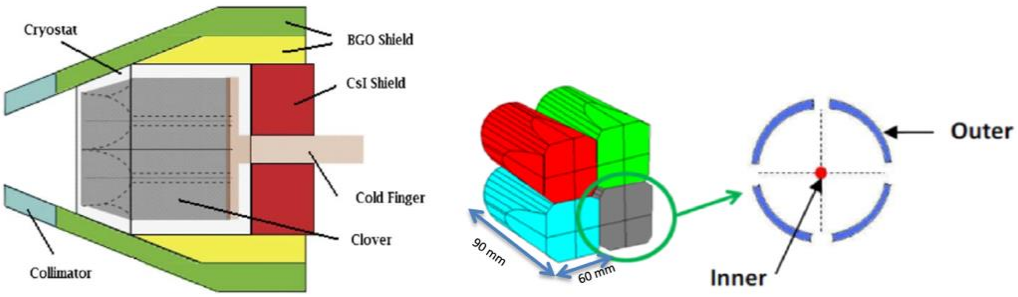

Figure 3. Left: Detail of the segmented CLOVER Ge detector crystal. Right: Zoom-in on segmented crystals.

Electronic detection systems significantly affect the quality of test data. New engineering matrix structures use high-speed analog-to-digital (A/D) devices, high-speed optical data transfers, and reconfigurable logic devices in the front electronics to add channels and complex processing algorithms [21]. Therefore, NUMEXO2 provides a common solution for more detection systems, reducing time and resources.

NUMEXO2 [22] serves as the central component within the NEDA front-end electronics. Collaboratively developed with GANIL, the NUMEXO2 digitizer and pre-processing system offer a unified solution for various detection systems, ultimately streamlining time and resource allocation. The primary functions of the digitizer encompass A/D conversion, data pre-processing, interfacing with the Global Trigger System GTS system, and managing communication links for up to 16 channels. This system comprises a motherboard and a quartet of FADC mezzanines, each responsible for A/D conversion in four channels. The NUMEXO2 digital electronics can capture 14-bit data at 200 Msps (Megasamples per second) and has a data transfer rate of 100–200 MHz. NUMEXO2's adaptability is achieved through its utilization of Field-Programmable Gate Arrays FPGAs, simplifying the design of firmware algorithms. Specifically, NUMEXO2 incorporates two high-performance FPGAs, namely a Virtex-6 and a Virtex-5 by Xilinx. Figure 4 provides an overview of the central NUMEXO2 block diagram, featuring the FPGAs, Flash Analog Digital Converter FADC mezzanine components, and communication links [22].

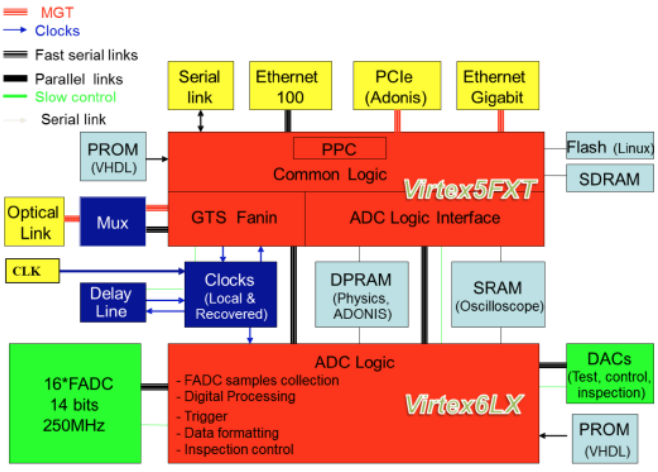

Figure 4. NUMEXO2 general block diagram [20].

3. RESULTS AND DISCUSSION

A general requirement for scientific data processing is to detect signal peaks and measure the peak heights to obtain information about the properties of the peaks, which in turn provides information about the underlying physical system. The energy spectrum of gamma rays is obtained from the detectors, and the peaks in this spectrum are then detected and analyzed. The task is to identify the peaks and measure their locations, widths, and heights. The calibration process is critical for accurately associating energies with peak locations in the spectrum.

3.1 Calibration Procedure

In this study, we used a ^{152}Eu radioactive source for the calibration of the EXOGAM2 detectors. This source emits gamma rays at two distinct energy levels: 344. 785 keV and 1408 keV. These well-known gamma lines were employed to calibrate the detectors. The calibration coefficients were derived by fitting the energy peaks corresponding to these gamma lines and using the coefficients of the line equation. The energy calibration was performed for two EXOGAM2 detectors, for 8 HpGe crystals. The third degree of the equation $E_{i=} \sum_n a_n \, c_i^n$ was used to calibrate the EXOGAM2 detectors.

3.2 Peak Fitting Process

The peak fitting process was conducted using the ROOT program, a widely used tool in nuclear physics. ROOT provides a versatile environment for data analysis, offering tools for fitting energy spectra, which contain intense low and high-energy peaks. By fitting the energy peaks, we were able to determine the mean energy values for each crystal. Aligning these mean energy values with the reference energies from the ^{152}Eu radioactive source ensured that each gamma energy was correctly positioned.
For each crystal, correction coefficient values constructed using the mean energy values obtained from the peak fitting method to align them with the known energies of ^{152}Eu. Therefore, the data was prepared for analysis to obtain the energy resolution for EXOGAM2 with newly developed NUMEXO2 electronic.

3.3 Energy Resolution Analysis

The energy resolution of each crystal in the EXOGAM2 system was determined based on the FWHM of energy peaks. The FWHM is a standard metric used to quantify the distribution at half width of the peak. The lower the FWHM value, the higher the sensitivity level of the detector, allowing the separation of closely related gamma energies.
The energy resolution values for each crystal were calculated at both the low-energy peak (344.785 keV) and the high-energy peak (1408 keV) from the ^{152}Eu source. Figure 5 shows measured FWHM values as an example for the second crystal of EXOGAM2 for ^{152}Eu energies at 344.785 keV and 1408 keV.
The values for all the crystals for EXOGAM were obtained using the ROOT software, and the results are summarized in Table 1 [23].

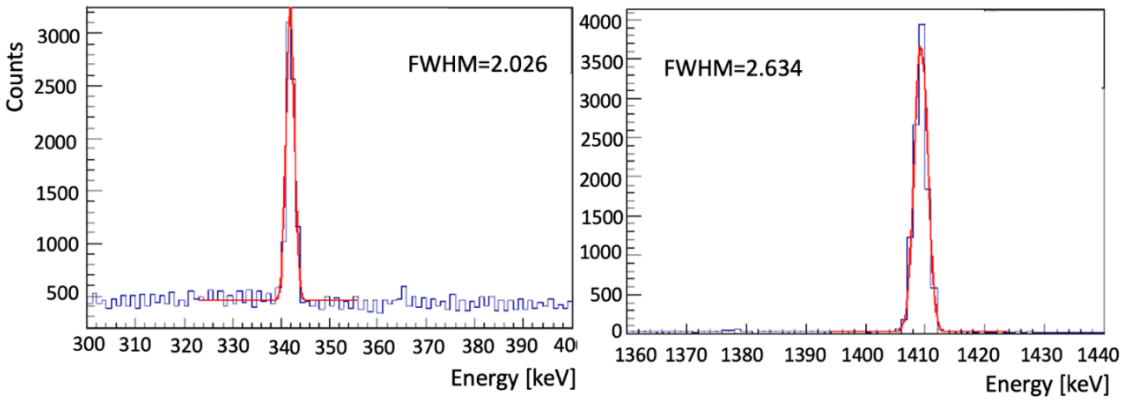

Figure 5. Examples of peak fitting from the radioactive ^{152}Eu calibration source are shown in the left (344.785 keV) and right (1408 keV) panels [23].

Table 1: Energy resolution values for each crystal in the EXOGAM2 system at 344.785 keV and 1408 keV [23].

Crystal Name	Energy resolution for the low energy region-344.785 keV (FWHM)	Energy resolution for the high energy region-1408 keV (FWHM)
1.EXOGAM2-1	2.087	2.684
1.EXOGAM2-2	2.026	2.634
1.EXOGAM2-3	2.004	2.573
1.EXOGAM2-4	3.168	2.938
2.EXOGAM2-1	2.411	2.670
2.EXOGAM2-2	2.409	2.677
2.EXOGAM2-3	2.813	3.410
2.EXOGAM2-4	2.616	4.051

FWHM values for all the crystals of EXOGAM2 shows the energy resolution of EXOGAM2 with NUMEXO2 digitizer determines how accurately it can measure the energy of these gamma rays. Moreover, how distinguish between gamma rays with very close energy levels, providing more precise information about the source. Therefore, the energy resolution which are obtained from the calculation of FWHM are listed in Table 1 for relatively low and high energies of ^{152}Eu. The results indicate that the energy resolution deteriorates as the energy value increases, which is a characteristic property of high-energy efficient detectors. However, certain crystals showed unexpected results, which may require further investigation.

4. CONCLUSION

In this study, we presented the calibration process of the EXOGAM2 conventional gamma detector system using the newly developed NUMEXO2 digital electronic device. Calibration was performed with a ^{152}Eu radioactive source emitting gamma rays at two distinct energy levels. Calibration coefficients were derived from the line equation coefficients obtained by fitting the energy peaks corresponding to these gamma lines.

The energy resolution of each crystal in the EXOGAM2 system was determined based on the FWHM of energy peaks. The results indicated that the energy resolution values for the low-energy branch exhibited reasonable results. However, for high energies, the resolution was not as favorable as for low energies. Notably, the resolution of the 4th, 7th, and 8th crystals at both low and high energy levels displayed unexpected outcomes, necessitating further examination in future experiments with this detector.

Nevertheless, these findings suggest that the use of the NUMEXO2 digital electronic device did not negatively impact the energy resolution of the detectors.

Overall, integrating the NUMEXO2 digital electronic device into the EXOGAM2 detector system facilitates efficient data acquisition at high counting rates, making it a valuable tool for nuclear physics experiments. Further investigations and refinements may be necessary to address unexpected results in certain crystals and optimize the system for specific research objectives.

SIMILARITY RATE: 11 %

CONFLICT of INTEREST

The authors declared that they have no known conflict of interest.

REFERENCES

[1] FJ Egea Canet et al. A new front-end high-resolution sampling board for the new generation electronics of EXOGAM2 and NEDA detectors. IEEE Transactions on Nuclear Science, 62(3):1056–1062, 2015.

[2] G. de France. Exogam detectors. [Online]. Available: http://pro.ganilspiral2. eu/laboratory/detectors/exogam/exogam-detectors.

[3] G De Angelis, A Bracco, and D Curien. The EUROBALL gamma ray detector array. Europhysics news, 34(5):181–185, 2003.
[4] FS Goulding, DA Landis, N Madden, M Maier, and H Yaver. Gammasphere. Overview of detector and signal processing system. In Nuclear Science Symposium and Medical Imaging Conference Record, 1995., 1995 IEEE, volume 1, pages 432–436. IEEE, 1995.
[5] J Eberth, G Pascovici, HG Thomas, N Warr, D Weißhaar, D Habs, P Reiter, P Thirolf, D Schwalm, C Gund, et al. Miniball: A gamma-ray spectrometer with position sensitive ge detectors for nuclear structure studies at rex-isolde. In AIP Conference Proceedings, volume 656, pages 349–356. AIP, 2003.
[6] S Akkoyun, Alejandro Algora, B Alikhani, F Ameil, G De Angelis, L Arnold, A Astier, Ayse Atac¸, Y Aubert, C Aufranc, et al. Agata advanced gamma tracking array. Nuclear Instruments and Methods in Physics Research Section A: Accelerators,Spectrometers, Detectors and Associated Equipment, 668:26–58, 2012.
[7] CW Beausang. Greta: the gamma-ray energy-tracking array. status of the development and physics opportunities. Nuclear Instruments and Methods in Physics Research Section B: Beam Interactions with Materials and Atoms, 204:666–670, 2003.
[8] PT Greenlees. on behalf of the jurogam and great collabs. Nucl. Phys. A, 787:507c, 2007.
[9] DG Sarantites, W Reviol, CJ Chiara, RJ Charity, LG Sobotka, M Devlin, M Furlotti, OL Pechenaya, J Elson, P Hausladen, et al. Neutron shell: a high efficiency array of neutron detectors for gamma-ray spectroscopic studies with gammasphere. Nuclear Instruments and Methods in Physics Research Section A: Accelerators, Spectrometers, Detectors and Associated Equipment, 530(3):473–492, 2004.
[10] J. Nyberg. Neutron wall. [Online]. Available: http://egpworkshop.in2p3.fr/docs/Talks-Mardi/nwall-jn.pdf., 27-30 May 2008.
[11] O Skeppstedt, HA Roth, L Lindstr¨om, R Wadsworth, I Hibbert, N Kelsall, D Jenkins, H Grawe, M G´orska, M Moszynski, et al. The EUROBALL neutron wall–design and performance tests of neutron detectors. Nuclear Instruments and Methods in Physics Research Section A: Accelerators, Spectrometers, Detectors and Associated Equipment, 421(3):531–541, 1999.
[12] J.J. Valiente-Dobon. Neda - neutron detector array. [Online]. Available: http://www.mi.infn.it/WSBormio-Milano2012/Doc/TALK/Dobon-Bormio12-web.pdf., 22-25 February 2012.
[13] G Jaworski, M Palacz, Johan Nyberg, G De Angelis, G De France, A Di Nitto, J Egea, MN Erduran, S Ertürk, E Farnea, et al. Monte carlo simulation of a single detector unit for the neutron detector array NEDA. Nuclear Instruments and Methods in Physics Research Section A: Accelerators, Spectrometers, Detectors and Associated Equipment, 673:64–72, 2012.
[14] BM Nyako et al. Performance of the diamant detector at ganil and plans for improvements.ATOMKI laboratory: for the DIAMANT collaboration,(unpublished), 2007.
[15] RD Baertsch and RN Hall. Gamma ray detectors made from high purity germanium. IEEE Transactions on Nuclear Science, 17(3):235–240, 1970.
[16] WL Hansen. High-purity germanium crystal growing. Nuclear Instruments and Methods, 94(2):377–380, 1971.
[17] J Llacer. Planar and coaxial high purity germanium radiation detectors. Nuclear Instruments and Methods, 98(2):259–268, 1972.
[18] F Azaiez. Exogam: gamma ray spectrometer for radioactive beams. Nuclear Physics A, 654(1):1003c–1008c, 1999.
[19] J Simpson, F Azaiez, G De France, J Fouan, J Gerl, R Julin, W Korten, PJ Nolan, BM Nyako, G Sletten, et al. The exogam array: a radioactive beam gamma-ray spectrometer. Acta Physica Hungarica, New Series, Heavy Ion Physics, 11:159–188, 2000.
[20] Glenn F Knoll. Radiation detection and measurement. John Wiley & Sons, 2010.
[21] FJ Egea Canet et al. A new front-end high-resolution sampling board for the new generation electronics of EXOGAM2 and NEDA detectors. IEEE Transactions on Nuclear Science, 62(3):1056–1062, 2015.
[22] M Tripon. EXOGAM2 technical specifications, 2012.
[23] Şahin Elif, "Adaptation Of Digital Electronic Into Detector Systems NUMEXO2 In Exotic Nuclei Research", Master Thesis, İzmir Institute of Technology, 2017.

Eurasian Journal of Science Engineering and Technology

Research Article

A NEWLY RECORDED GENUS FOR TURKISH SPIDER FAUNA (ARANEAE: HAHNIIDAE)

Osman SEYYAR [1,*], Tuncay TÜRKEŞ[2], Hakan DEMİR[3]

[1,2,3] *Nigde Omer Halisdemir University, Science and Arts Faculty, Department of Biology, 51240, Niğde, Türkiye*

ABSTRACT

The spider species *Mastigusa arietina* (Thorell, 1871) together with its genus *Mastigusa* Menge, 1854, was found in northwest of Anatolia and represent new record for Turkish spider fauna. Digital photographs of genitalia and habitus and its locality knowledges are presented.

Keywords: Hahniidae, New record, Anatolia, Fauna

1. INTRODUCTION

Hahniidae is a small spider family with about 357 described species from 24 genera. *Mastigusa* Menge, 1854 is one of the smallest genus in the family. Currently it includes only 3 species distributed worldwide [1]. Turkish hahnid fauna includes 8 species in 4 genera, but there is no species of *Mastigusa* have been known from Türkiye [2-4]. Recently we found two specimens of *Mastigusa arietina* (Thorell, 1871) from Türkiye. Both species and genus new to country. The main purpose of the present work is to new datas for Turkish Spider Fauna.

2. MATERIAL AND METHOD

In this study, only two males specimens were collected from Giresun provinces in Black Sea Region in Türkiye in 2008 (Fig. 1). Examined specimens were preserved in 70% ethanol and deposited in the Arachnology Museum of Niğde Ömer Halisdemir University (NOHUAM). In the identification, Locket & Millidge 1953; Roberts, 1995 and Wunderlich, 1986 were consulted [5-7]. The identification was made by means of a SZX61. The map of the distribution was prepared using SimpleMappr programs [8].

Figure 1. Collecting locality of *Mastigusa arietina* (Thorell, 1871) (red star) in Türkiye.

* Corresponding author, e-mail: oseyyar@ohu.edu.tr, (O. Seyyar)
Recieved: 24.07.2023 Accepted: 07.09.2023
doi: 10.55696/ejset.1332180

3. RESULTS AND DISCUSSION

***Mastigusa arietina* (Thorell, 1871) Figs (2,3)**

Identification and description: Roberts, 1995

Comments: This species distributed in west Palaearctic. Both species and genus new to Türkiye. Only one female of this species are known from the Asia [9]. This is the first record of male of this species from Asia. It is predicted that careful searching will reveal further localities in Anatolia, as well as other parts of Asia.

Taxonomic references

Cryphoeca arietina Thorell, 1871.
Cicurina impudica Simon, 1875.
Cicurina arietina Simon, 1875.
Tetrilus diversus Simon, 1937.
Tetrilus arietinus Bristowe, 1939.
Mastigusa arietina Almquist, 2006.
Mastigusa arietina Zamani et al., 2020.

Collecting specimens: Giresun Province: Dereli district, Uzundere village (40°32'49.6"N 38°21'47.2"E), 26.VIII.2008 (2♂♂); Leg. Tuncay TÜRKEŞ.

Figure 2. Male habitus of *Mastigusa arietina* (Thorell, 1871) (Palp dissected)

Figure 3. Male genitalia of *Mastigusa arietina* (Thorell, 1871): A-Palp (ventral), B-Palp (retrolateral)

SIMILARITY RATE: 15%

CONFLICT of INTEREST

The authors declared that they have no known conflict of interest.

REFERENCES

[1] World Spider Catalog (2023). World Spider Catalog. Version 24.5. Natural History Museum Bern, online at http://wsc.nmbe.ch, accessed on {15. VII.2023}. doi: 10.24436/2

[2] A. Topçu, H. Demir, and O. Seyyar, "A checklist of the spiders of Turkey," *Serket*, vol. 9, no. 4, pp. 109-140, 2005.

[3] H. Demir and O. Seyyar, "Annotated checklist of the spiders of Turkey," *Munis Entomology and Zoology*, vol. 12, no. 2, pp. 433-469, 2017.

[4] T. Danışman, K.B. Kunt, R.S. Özkütük, and İ. Coşar, "The Checklist of the Spiders of Turkey, Version 2023," 2023. [Online]. Available: http://www.spidersofturkey.info. [Accessed: Apr. 14, 2023].

[5] G.H. Locket, and A.F. Millidge, *British Spiders.* London: Ray Society, 1953.

[6] J. Wunderlich, *Spinnenfauna gestern und heute: Fossile Spinnen in Bernstein und ihre heute lebenden Verwandten*. Wiesbaden: Quelle & Meyer, 1986.

[7] M. J. Roberts, *Collins Field Guide: Spiders of Britain & Northern Europe*. London: HarperCollins, 1985.

[8] Shorthouse D.P. 2010. SimpleMappr, an online tool to produce publication-quality point maps. http://www.simplemappr,net [Accessed: Apr. 14, 2023].

[9] A. Zamani, D. Dimitrov, I. Weiss, S. Alimohammadi, R. Rafiei-Jahed, S. L. Esyunin, M. Moradmand, M. Chatzaki, and Y. M. Marusik, "New data on the spider fauna of Iran (Arachnida: Araneae), part VII," *Arachnology*, vol. 18, pp. 569-591, 2020.

Eurasian Journal of Science Engineering and Technology

Research Article

THE MODIFIED OHM'S LAW AND ITS IMPLICATIONS FOR ELECTRICAL CIRCUIT ANALYSIS

Alex Mwololo KIMUYA[1*]

[1]*Department of Physical Science (Physics), Meru University of Science and Technology, Kenya*

ABSTRACT

Ohm's Law has long been a cornerstone of electrical engineering, providing a linear relationship between voltage, current, and resistance that has underpinned modern circuit analysis. However, as technology advances and philosophical inquiries deepen, the limitations of this venerable law have become evident, particularly in scenarios involving near-zero resistance. This paper introduces a novel formulation-the modified Ohm's Law; that not only rectifies the pitfalls of the conventional law but also harmonizes physics with philosophical principles. Motivated by the perplexing issue of predicting infinite current at zero resistance and the philosophical implications of deriving infinity from the finite, the modified equation serves as a bridge between empirical insights and logical coherence. Through rigorous mathematical derivation, comprehensive theoretical examination, and scrupulous computational analysis, the accuracy and applicability of the modified Ohm's Law are not only demonstrated but also its suitability across a wide range of scenarios is revealed. These scenarios include semiconductor devices, high-current applications, and complex systems where the standard Ohm's Law falls short, offering a transformative perspective on the analysis of electrical circuitry. In reconciling scientific rigor with philosophical consistency, this paper advances our understanding of electrical circuitry and beckons a new era of precision in analysis. Further, the modified Ohm's Law paves the way for deeper explorations that resonate through the domains of physics and philosophy, reshaping the landscape of our understanding.

Keywords: Modified Ohm's Law, Electrical circuit analysis, Non-linear behavior, Resistance, Exponential function, Short circuit, Philosophy of physics, Accuracy, Computational analysis

1. INTRODUCTION

Electricity, the backbone of modern civilization, has woven itself into the very fabric of our daily lives. The intricate networks of circuits power our homes, workplaces, and digital connections. At the core of understanding and harnessing this invisible force lies the Ohm's Law, a principle that has guided the domain of electrical engineering for generations [1-5]. However, as technological prowess evolves and our insights into the dynamics of circuits deepen, the limitations of this long-standing law have begun to emerge [6-9]. This paper embarks on a transformative journey, introducing an innovative formulation-the modified Ohm's Law-that not only addresses the deficiencies of the conventional law but also seeks to bridge the gap between scientific tenets and philosophical principles. For over a century, Ohm's Law ($V = IR$) has been the bedrock upon which engineers and scientists have built the edifice of electrical and electronics engineering [1], [3], [4], [10-12]. It's simple linear relationship between voltage (V), current (I), and resistance (R) has unlocked countless possibilities, enabling the design, analysis, and optimization of circuits that underpin our modern way of life. Yet, as technological frontiers advance, so too does our scrutiny of the foundations upon which they rest. Amidst these advancements, the conventional Ohm's Law harbors an intriguing paradox; it suggests that in an electrical conductor, when the resistance (R) approaches zero, the current (I) becomes infinite [5]. This assertion, while it may be mathematically coherent, raises profound questions about the very nature of our reality. It challenges our experiential understanding and delves into the domain of philosophical paradoxes [13], [14], where the notion of deriving infinity from the finite is at odds with our intuitive grasp of the world. This paper embarks on a quest to address this conundrum and proposes an alternative formulation, the modified Ohm's Law that harmonizes the empirical with the philosophical, rectifying the tensions between the mathematical characterization of the Ohm's Law and reality. Guided by the principles of scientific advancement and philosophical coherence, this paper navigates the intricate terrain of electrical circuitry. It seeks to redefine the boundaries of our understanding by examining the motivations behind modifying the standard Ohm's Law and unearthing the theoretical underpinnings of the modified equation. Furthermore, it employs computational analysis to unravel the practical implications of this new formulation across diverse scenarios. From semiconductor devices to high-current applications, the modified Ohm's Law promises a paradigm shift in the way we approach electrical circuit analysis.

* Corresponding author, e-mail: alexkimuya23@gmail.com (A. M. Kimuya)
Recieved: 09.10.2023 Accepted: 10.11.2023
doi: 10.55696/ejset.1373552

2. A PHILOSOPHICAL AND THEORETICAL EXPLORATION

In light of these intricate considerations, it becomes evident that the notion of resistance reaching zero is fraught with challenges that extend beyond the domain of physics alone. The paradoxes and inconsistencies that emerge when grappling with the concept of infinite current at zero resistance demand a holistic exploration that delves into both theoretical and philosophical dimensions.

2.1 The Infinite Current Fallacy

The standard Ohm's Law, while remarkably successful in predicting and explaining electrical behavior, harbors a perplexing fallacy that challenges both physics and intuition. According to the standard Ohm's Law, when resistance approaches zero, the resulting current tends toward infinity [5]. This concept, however, contradicts fundamental experiential understanding. Practical scenarios exist where infinitely large currents are not observed, and this inconsistency creates a rift between theoretical predictions and empirical observations. This paper delves into this apparent paradox and investigates its implications. Confronting this issue head-on, the goal is to rectify the discrepancy between theoretical constructs and the physical world, paving the way for a more coherent understanding of electrical circuit behavior.

2.2 The Philosophy of Something from Nothing

The claim that zero resistance results in an infinite current presents a philosophical puzzle that extends beyond the domain of physics comprehension. This concept appears to attribute an infinite effect from a finite cause, challenging the principles of causality and the continuity of physical phenomena. Furthermore, the suggestion that an infinite quantity could originate from a finite source, or perhaps even from nothing, is perplexing and defies our intuitions about magnitude and the nature of infinite quantities (in a broader sense, it contradicts our understanding that something cannot emerge from nothing [13], [14]). Such a contradiction raises profound philosophical questions about the nature of reality, causation, and the very foundation of physical laws [15-17]. Introducing the modified Ohm's Law aims to address these philosophical tensions. The exponential relationship in the modified equation inherently restricts the notion of infinite current at zero resistance, aligning more harmoniously with our philosophical understanding of causality and the limitations of deriving limitless quantities from finite ones.

2.3 Reconsidering $R = 0$ In Classical Settings

The assumption that resistance can ever exactly reach zero is examined from both classical and modern perspectives. Classical physics holds that infinitesimal quantities have definite values, but modern theories such as quantum mechanics introduce uncertainty even at the smallest scales [18]. In the context of electrical circuits, the assumption of zero resistance triggers paradoxes and inconsistencies that hinder our ability to accurately model real-world behavior. This section endeavors to challenge the idea that, when dealing with a conductor, electrical resistance denoted as R can equal zero. The perspective of zero resistance, as presented in [19], is adjusted and embraced. The fundamental current formulation derived from Ohm's law is presented in equation (1):

$$I = \frac{V}{R} \tag{1}$$

In the ideal (mathematical) form, equation (1) suggests the perplexing possibility that:

$$I = \frac{V}{0} = \infty \tag{2}$$

This implication raises the question of deriving an infinite quantity from a finite physical relationship. The ensuing discussion aims to provide a coherent objection to this perspective and, in doing so, challenges the plausibility of the mathematical assertion that electrical resistance in a conductor can ever be $R = 0$.

The foundational definition of electrical resistance is commonly expressed as:

$$R = \rho \frac{L}{A} \tag{3}$$

To explore the notion that $R = 0$, let us consider two hypothetical instances:

Premise 1 (When $\mathbf{L = 0 \Rightarrow A = 0}$). Considering the geometric property of the conductor's cross-sectional area $A = \pi r^2$, where r is the radius, a relationship between L and r can be established. Thus, when, $L = 0$, it would imply that $r = 0$ suggesting the existence of electrical conductors without any measurable cross-sectional area in their geometry. This leads to the curious mathematical result:

$$R = \rho \frac{0}{0} = \infty \tag{4}$$

Equation (4) demonstrates that if the hypothetical relations $L = r = 0$ were valid, the electrical resistance of the conductor would tend towards infinity, rather than zero. This scenario is counterintuitive, as an infinitely large electrical resistance contradicts the existence of an electrical conductor. A more accurate interpretation could be that in the case of an open circuit, resistance tends towards infinity, as posited in studies involving electrical voltage and current using Norton-Thevenin relations [20]. This paper acknowledges the significance of geometry in influencing electrical resistance.

Premise 2 (When either $\boldsymbol{\rho = 0}$). Setting $\rho = 0$ in equation (3) results in $R = 0$, which might seem plausible. However, this assertion holds ambiguous physical significance and is subject to challenge. In this context, ρ represents the inherent resistivity of the electrical conductor, and asserting $\rho = 0$ implies a conductor devoid of resistivity property or material. This proposition contradicts the reality, as materials inherently possess resistive properties. Consequently, it is rational to conclude that material resistance equals zero only in the absence of conducting material or when no voltage and current source is present (with the consideration that any power source inherently possesses some resistance, as studied in the context of Norton-Thevenin concepts [20]). From a physics standpoint, the assertion that $(R = 0)$ contradicts the fundamental principles governing electrical behavior. Electrical resistance is a measure of how a conductor opposes the flow of electric current. This opposition arises due to various factors, including collisions between electrons and lattice vibrations within the conductor's atomic structure. These interactions inherently contribute to the resistive properties of materials. Proposing that $(R = 0)$ implies the absence of these interactions altogether, which contradicts the very nature of conductive materials. Even in the most ideal conditions, materials possess inherent properties that introduce a level of resistance, rendering the concept of zero resistance implausible. Beyond the domain of physics, the notion of zero resistance carries philosophical implications that challenge the very foundations of our understanding of causality and existence. The philosophical principle of causality asserts that an effect arises from a cause [15-17]. The assertion of infinite current $(I = \infty)$ corresponding to zero resistance $(R = 0)$ defies this principle by suggesting an effect without a cause-a finite voltage (V) seemingly generating an infinite result. This contradicts the inherent order and logic that underpin our conception of reality. Further complicating matters is the concept of idealization, often encountered in theoretical models. In the idealization of $(R = 0)$, we encounter a scenario where the resistance of a conductor is perceived to vanish under perfect conditions. However, the idealization of zero resistance becomes an exercise in abstraction divorced from practical realities. In the physical world, no conductor can be completely devoid of resistive effects. Even superconductors, often cited as examples of extremely low resistance, possess non-zero resistance at finite temperatures. This serves as a reminder that real-world conditions introduce complexities that challenge idealized notions. The assumption that in ideal scenarios $(R = 0)$ leads to paradoxical outcomes. An infinite current suggests an unbounded flow of charge, potentially generating infinite energy. This paradox fundamentally contradicts conservation laws and energy principles. Infinite quantities arising from finite conditions undermine the coherent understanding of physical laws and mathematics. Generally, the proposal that $(R = 0)$ in electrical conductors encounters insurmountable challenges at both the physics and philosophical levels. The inherent resistive properties of materials, the violation of causality, the issues of idealization, and the paradoxical nature of infinite quantities all converge to discredit the plausibility of zero resistance. As such, the pursuit of an accurate description of electrical behavior necessitates a departure from the notion of $(R = 0)$ and a recognition of the complex interplay of physical and philosophical principles that govern our understanding of the universe.

3. DERİVATİON AND THEORETİCAL EXAMİNATİON OF THE MODİFİED OHM'S LAW

Having examined the limitations posed by the standard Ohm's Law and recognizing the need for a more accurate framework, the next step involves the mathematical derivation and theoretical underpinnings of the modified Ohm's Law. By introducing an exponential term to the equation, an attempt is made to present a consistent solution that addresses the intricacies present in situations with extremely low resistance values. Through this derivation, the goal is to establish a solid basis for the subsequent exploration of the modified Ohm's Law, shedding light on how this innovative formulation resolves the paradoxes and inconsistencies linked to resistance nearing zero.

3.1 Mathematical Derivation

To address the shortcomings of the standard Ohm's Law, a modified equation that redefines the relationship between resistance, current, and a parameter referred to as "short resistance", denoted as (R_{short}) is introduced. The standard Ohm's Law assumes a linear relationship between voltage and current, resulting in the erroneous implication of infinite current at zero resistance. The provided modified formulation, (equation 17), incorporates an exponential term that elegantly avoids this paradox.

To derive this equation, the section begins with the premise that resistance is a function of "short resistance" $(R = f(R_{short}))$. By incorporating an exponential term into the equation, resistance is prevented from ever reaching zero, thus ensuring that current remains finite. This derivation hinges on the understanding that exponential functions provide a powerful tool to model non-linear behavior, allowing us to navigate situations where resistance becomes extremely small.

To start off, imagine of an electrical short circuit model; then, consider the standard Ohm's Law, $V = I \times R$, where V is voltage, I is current, and R is resistance.

Again, consider a modified scenario where resistance (R) is not a constant, but a function of some parameter x, which could be a representation of some variables, for instance, the length of the conductor or the temperature, among the others outlined in section (5).

So, one can express R as $R = R(x)$ (4)

In this case, the standard Ohm's Law has been modified to become $V = I \times R(x)$ (5)

Assumption. To complete the derivation, it will be assumed that $R(x)$ can be expressed as an exponential function of x. I will then use the general form $R(x) = a \times e^{bx}$ (6)

Where a and b are constants, within the context of an electrical short circuit in an electrical conductor.

This assumption is justified by the non-linear behavior, rapid resistance changes, complex interactions, and the physical processes involved. The choice for the exponential relation $R(x) = a \times e^{bx}$ is further justified in (Appendix II).

Substituting the expression for $R(x)$ (equation 6), back into equation (5):

$I = \frac{V}{a \times e^{bx}}$ (7)

Further, I now let $I_0 = \frac{V}{a}$ be the current when $x = 0$. In other words, I_0 represents the current when resistance is at its reference value (R_0).

Using I_0 into equation (7) gives:

$I = I_0 \times \frac{1}{e^{bx}}$ (8)

Now, I will make a small change in the notation as follows.

İ will let R_{short} be the change in resistance from its reference value (R_0), so that $R_{short} = R(x) - R_0$ (9)

This means that $R(x) = R_0 + R_{short}$ (10)

Substituting $R(x)$ back into equation (8) leads to:

$I = I_0 \times \frac{1}{e^{b(R_0 + R_{short})}}$ (11)

Using the properties of exponential functions; $e^{a+b} = e^a \times e^b$, equation (11) can be rewritten as follows:

$I = I_0 \times \frac{1}{e^{b(R_0)} \times e^{b(R_{short})}}$ (12)

Notice that $e^{b(R_0)}$ is just a constant, so it can be represented as a, and $e^{b(R_{short})}$ is precisely the term in the modified Ohm's Law. Therefore:

$$I = I_0 \times \frac{1}{a \times e^{b(R_{short})}} \quad (13)$$

Equation (13) can be further simplified as follows:

$$I = \frac{I_0}{a} \times \frac{1}{e^{b(R_{short})}} \quad (14)$$

But since $\frac{I_0}{a}$ is simply a constant, I choose denote it as a in the modified Ohm's Law, resulting in:

$$I = a \times \frac{1}{e^{b(R_{short})}} \quad (15)$$

And equation (15) simplifies to:

$$I = a \times e^{-b(R_{short})} \quad (16)$$

The hope here is to have the current increase exponentially as resistance decreases. So, the focus now is to adjust the sign of b to make it positive, and denote b as $\frac{1}{R_0}$:

$$I_{modified} = a \times e^{\frac{R_{short}}{R_0}} \quad (17)$$

Equation (17) completes the derivation of the modified Ohm's law equation $\left(I_{modified} = a \times e^{\frac{R_{short}}{R_0}}\right)$ from an electrical conductor model, ensuring that as resistance decreases (R_{short} gets smaller), the current increases exponentially

Through the development of the modified Ohm's Law (equation 17), the intent is to bridge the gap between classical assumptions and the complexities of modern realities in electrical circuit analysis. This innovative formulation, characterized by the introduction of an exponential term, seeks to rectify the inherent limitations associated with the notion of resistance approaching zero. The intention is to provide a comprehensive and accurate predictive model that remains applicable across a broader spectrum of scenarios. Classical theories often assume linear relationships between voltage, current, and resistance, leading to the belief that resistance can potentially vanish. However, the modified Ohm's Law is specifically engineered to address the pitfalls and paradoxes arising from this assumption. By introducing the exponential term, an explicit acknowledgment is made that resistance cannot truly reach zero in practical situations. This acknowledgement aligns with experiential understanding that even materials touted as superconductors exhibit resistance at finite temperatures. Additionally, the core of the presented approach lies in striking a balance between the mathematical elegance of the law and its empirical validity. The exponential form of the modified Ohm's Law offers a more realistic depiction of resistance behavior during conditions that approach very low values. This accounts for the inherent complexities and interplay of factors that can influence resistance in real-world scenarios, such as thermal effects, material properties, and electromagnetic interactions. Thorough the subsequent sections, it is established that unlike the standard Ohm's Law, the proposed equation does not project the erroneous notion of infinite current resulting from zero resistance. The modified Ohm's Law, therefore, emerges as a thoughtful and substantiated response to the limitations exposed by classical assumptions. With the incorporation of the exponential term, the shortcomings of linear models are addressed, providing a robust framework that better aligns with both theoretical insights and practical observations.

3.2 Applying The Modified Ohm's Law

The modified Ohm's Law, given by equation (17) provides a more accurate representation of current behavior when resistance values are extremely small. It's particularly useful in scenarios where standard Ohm's Law might yield unrealistic results, such as when resistance approaches zero.

3.2.1 Breakdown of The Modified Ohm's Law Components

***R_{short}* (Resistance Variation).** This parameter is a fundamental component in the analysis of the modified Ohm's Law. It represents the variable resistance under investigation and serves as a crucial element in modeling how resistance behaves in different electrical circuit scenarios. By varying R_{short} across a range of resistance values, one gains insights into how resistance

changes as it approaches extremely low values. This parameter allows one to explore real-world situations where low resistance values might be encountered, such as in semiconductor devices or high-current applications.

a* (Current Scaling Factor).** This constant determines the scaling of the current. It is calculated as the voltage divided by the reference resistance $\left(\boldsymbol{a} = \frac{\boldsymbol{V}}{\mathbf{R_0}}\right)$. Adjusting "a***" can control the rate of increase in current as resistance decreases. Applying the modified Ohm's law, one can experiment with different values of ***a*** to observe how current changes with resistance.

The constant "***a***" plays a pivotal role in the modified Ohm's Law. It determines the scaling of current based on the reference resistance "$\mathbf{R_0}$", and it is calculated as the voltage divided by $\mathbf{R_0}$ $\left(\boldsymbol{a} = \frac{\boldsymbol{V}}{\mathbf{R_0}}\right)$. Adjusting "***a***" enables us to control the rate of increase in current as resistance decreases. In practical terms, this parameter allows us to fine-tune the behavior of current in response to changes in resistance. Through experimenting with different values of "***a***", we can observe how current varies and adapts to different resistance scenarios, thus offering valuable insights into circuit behavior.

R_0* (Reference Resistance).** This is a constant that establishes the reference resistance of the circuit. It serves as a point of comparison for calculating the scaling factor "a***". Adjusting "$\boldsymbol{R_0}$" has a direct impact on the overall magnitude of the current. Larger "$\boldsymbol{R_0}$" values result in smaller current values for a given resistance. This parameter allows us to explore the effects of reference resistance on current magnitude and provides a means to understand how resistance behavior is influenced by different reference points

The parameter *x*. The parameter "***x***" introduces additional variables and factors that can affect the behavior of resistance during a short circuit. These factors provide a more comprehensive understanding of how resistance changes in response to different conditions and scenarios. The (Appendix I) section provides an array of the factors that this parameter can model.

3.3 Comparing Standard and Modified Ohm's Laws-A Graphical Insight

This section provides compared relationship between the standard Ohm's Law $(I_{standard})$ and the modified Ohm's Law $(I_{modified})$ through a graphical representation. Figure (1) offers a visual depiction of the intricate interplay between resistance and current as dictated by these two fundamental laws. The x-axis is dedicated to the varying resistance values (R_{short}), while the y-axis quantifies the computed currents (I) for each resistance value. In this visualization, the blue line symbolizes the predictions of the standard Ohm's Law, whereas the red line signifies the outcomes of the modified Ohm's Law. Upon scrutiny of figure (1), a notable trend emerges; as resistance (R_{short}) diminishes, the current (I) exhibits a profound surge in accordance with the modified Ohm's Law $(I_{modified})$. In stark contrast, adherence to the standard Ohm's Law $(I_{standard})$ leads to the current escalating towards unrealistic and potentially infinite magnitudes. A distinctive feature of the modified Ohm's Law is its incorporation of an exponential term, effectively curbing the propensity of the current to spiral into the domain of impractical values as resistance dwindles. Figure (1) unequivocally accentuates the advantageous attributes of the modified Ohm's Law in scenarios characterized by extremely low resistance, where conventional applications of the standard Ohm's Law falter.

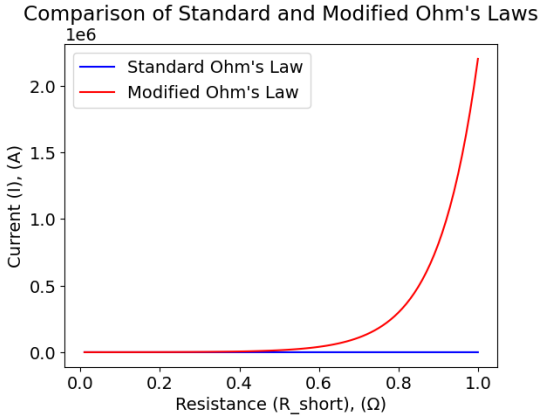

Figure 1. Comparison of Standard and Modified Ohm's Laws:
(The figure illustrates a comparison between the current calculated using the standard Ohm's Law (blue line) and the modified Ohm's Law (red line). The x-axis represents varying resistance values (R_{short}), while the y-axis represents the corresponding calculated currents (I)).

4. VALİDATİNG THE MODİFİED EQUATİON

With the theoretical foundation of the modified Ohm's Law laid out, the focus now shifts towards its practical validation. This section delves into the essential process of empirically substantiating the claims made regarding the modified equation's superiority over its standard counterpart. Various computational analyses are employed to investigate real-world situations and assess the performance of the modified Ohm's Law when confronting the intricacies and subtleties inherent in electrical circuit behavior.

4.1 Low-Resistance Measurements

In scenarios of low-resistance measurements, the modified Ohm's Law shines by accounting for contact and lead resistances that often skew results. Through simulations, this section demonstrates scenarios where the standard equation deviates from actual measurements due to the presence of these non-linearities. The modified equation, with its exponential term advantages, aligns more closely with the observed behavior, allowing for accurate estimation of resistance and current even in the presence of non-ideal elements.

Example. Consider a circuit with a known voltage ($V = 10\ V$), a known contact resistance ($R_{contact} = 0.1\Omega$), and a known lead resistance ($R_{lead} = 0.2\Omega$). The goal is to calculate the current flowing through the circuit using both the standard Ohm's Law and the modified Ohm's Law, taking into account the non-ideal elements. (Use Reference Resistance, $R_0 = 0.01\Omega$)

Given. Voltage, $V = 10\ V$, Contact Resistance, $R_{contact} = 0.1\Omega$, Lead Resistance, $R_{lead} = 0.2\Omega$, and Reference Resistance, $R_0 = 0.01\Omega$.

Step 1: Calculate Combined Resistance
The combined resistance of contact and lead can be calculated by summing the individual resistances:

$$R_{short} = R_{contact} + R_{lead} = 0.1\Omega + 0.2\Omega = 0.3\Omega$$

Step 2: Calculate Current using Standard Ohm's Law
Using the standard Ohm's Law equation; $I = \frac{V}{R}$, where $R = R_{short}$.

$$I_{standard} = \frac{V}{R_{short}} = \frac{10V}{0.3\Omega} \cong 33.333333333333333A$$

Step 3: Calculate Current using Modified Ohm's Law
In the modified Ohm's Law equation; $I_{modified} = a \times e^{\frac{R_{short}}{R_0}}$, where $a = \frac{V}{R_0}$.
$a = \frac{10V}{0.01\Omega} = 1000\frac{V}{\Omega}$

Substituting the values into the modified Ohm's Law equation;
$I_{modified} = 1000 \times e^{\frac{0.3\Omega}{0.01\Omega}} = 1.0686258935115146e + 16A$

Comparing the results;
- Current using standard Ohm's Law: $I_{standard} \approx 33.333333333333333A$
- Current using modified Ohm's Law: $I_{modified} \approx 1.0686258935115146e + 16A$

The modified Ohm's Law provides a significantly higher current estimate due to its exponential term that accounts for the non-ideal elements (contact and lead resistances). This illustrates how the modified equation aligns more closely with the observed behavior in low-resistance measurement scenarios.

4.2 High-Current Applications

Shifting focus towards high-current applications, one encounter situations where small resistance values result in unrealistic outcomes when using the standard Ohm's Law. Computational simulations are employed to demonstrate scenarios in which the

adjusted equation avoids the current approaching infinity, thereby guaranteeing that resistance and voltage maintain finite values. This feature enhances safety, preventing catastrophic failures in high-current circuits and power systems.

Example. Consider a scenario in which a voltage source of $100V$ is connected to an electrical circuit. The reference resistance of the circuit is 0.001Ω. Using both the standard Ohm's Law and the modified Ohm's Law, calculate and compare the current flowing through the circuit in a high-current application, where small resistance values can lead to unrealistic outcomes.

Given. Voltage, $V = 100V$, Resistance, $R = 0.001\Omega$ (Reference resistance)

Step 1: Calculate Current using Standard Ohm's Law
Using the standard Ohm's Law equation, $I = \frac{V}{R}$;

$$I_{standard} = \frac{V}{R} = \frac{100V}{0.001\Omega} = 100000A$$

Step 2: Calculate Current using Modified Ohm's Law
In the modified Ohm's Law equation;

$I_{modified} = a \times e^{\frac{R_{short}}{R_0}}$, where $a = \frac{V}{R_0}$.
$a = \frac{100V}{0.001\Omega} = 100000\frac{V}{\Omega}$

Substituting the values into the modified Ohm's Law equation:
$I_{modified} = 100000 \times e^{\frac{0.001\Omega}{0.001\Omega}} = 271828A$

The discrepancy between the currents calculated using the standard Ohm's Law and the modified Ohm's Law arises from the intrinsic nature of the modified equation. The exponential term introduced in the modified Ohm's Law becomes increasingly significant as the resistance approaches zero. In the case of extremely low resistance values, as seen in this example (0.001Ω), the exponential term dominates the equation, leading to a substantial increase in the calculated current. As demonstrated by the example, the modified Ohm's Law prevents the current from approaching infinity and ensures that both resistance and voltage remain finite, thereby enhancing the safety and accuracy of predictions in high-current scenarios. Following this example, a visual representation of the computation is presented in figure (2). The simulation showcases the currents calculated using both the standard and modified Ohm's Laws across a range of resistance values. The depicted results provides a clear comparison between the two approaches, with the standard Ohm's Law shown in blue and the modified Ohm's Law in red. Figure (2) offers a visual insight into how the modified Ohm's Law curbs the unrealistic outcomes associated with extremely low resistance values in high-current applications, ensuring safer and more accurate predictions.

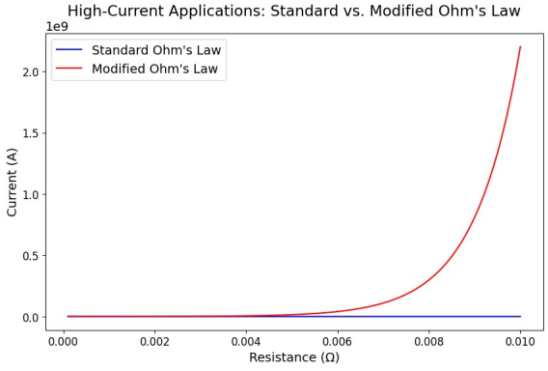

Figure 2. High-Current Applications: Comparison of Standard and Modified Ohm's Laws: The figure compares the currents calculated using the standard Ohm's Law (blue line) and the modified Ohm's Law (red line) across a range of resistance values. The x-axis represents varying resistance values in Ohms, while the y-axis represents the corresponding calculated currents in Amperes. The graph demonstrates the efficacy of the modified Ohm's Law in mitigating potential catastrophic failures caused by extremely low resistance values, showcasing a more accurate representation of current behavior in practical scenarios).

4.3 Comparative Analysis

The provided computational analysis involves a side-by-side comparison of predictions derived from the standard and modified equations. Through an examination of the disparities between them, the instances where the adjusted equation offers a more precise reflection of real-world behavior are underscored. These disparities serve as quantitative proof of concept, demonstrating that the modified Ohm's Law indeed offers a superior framework for analyzing circuits in various scenarios.

4.4 Enabling Advanced Design and Analysis

Through these computational simulations, the advanced circuit design and analysis opportunities are unveiled. Engineers can now leverage the modified equation to predict outcomes in scenarios previously marred by inaccuracies or paradoxes. Semiconductor devices, thermistors, varistors, and materials with non-uniform resistivities can all be more precisely analyzed and designed using the modified equation, fostering innovation and pushing the boundaries of what is possible in electrical engineering.

4.5 Strengthening The Bridge Between Theory and Practice

In presenting the results of the computational analysis, a connection is established between theoretical derivations and practical applications. The accuracy of the modified equation across various scenarios is showcased, reinforcing its role as a potent tool in contemporary electrical engineering science. The desired computational exploration reaffirms the alignment of the modified Ohm's Law with physical reality and paves the way for its smooth integration into the domain of circuit analysis and design.

5. DİSCUSSİON

Electrical short circuits, with their remarkably low resistance values, stand as quintessential examples that have captivated and perturbed the field of electrical engineering for decades, primarily due to their potential to trigger catastrophic system failures [3], [4], [10], [11], [21]. These occurrences underscore the vital significance of precise analysis and comprehensive understanding in addressing their complexities.

5.1 Anomalous Behavior and The Need for A New Approach

An electrical short circuit represents an extreme condition where the resistance of the conductor becomes extremely low [1], [5], often approaching zero. In such cases, the linear relationship assumed by the standard Ohm's Law ($V = IR$) may no longer accurately represent the behavior of the system. The exponential form $R(x) = a \times e^{bx}$ provides a mathematical framework that can better capture the non-linear behavior observed during a short circuit.

5.2 Drastic Changes In Resistance

During a short circuit, the resistance of the conductor experiences a significant reduction due to the creation of a low-resistance path [5]. This abrupt change in resistance corresponds to a rapid change in the behavior of the current flowing through the conductor. Exponential functions are known for their ability to describe sudden and significant changes, making them suitable candidates for modeling this kind of behavior.

5.3 Complex Interplay of Factors

A short circuit involves various complex factors, including the energetic instability, thermal effects, and electromagnetic interactions mentioned earlier [3], [5]. These factors can lead to non-linear variations in the current that are not adequately captured by a simple linear model. The exponential function provides a flexible form that can account for these complex interactions and their resulting effects on resistance and current.

5.4 Physical Processes Influencing Resistance

The exponential form of $R(x) = a \times e^{bx}$ aligns with certain physical processes that can influence resistance changes during a short circuit:

Thermal Effects. The drastic increase in current through a short circuit generates heat due to energy dissipation. Higher temperatures can lead to increased electron mobility and lower resistance. Exponential behavior can describe how resistance changes as temperature increases.

Material Properties. Exponential functions can represent material properties, such as changes in electron scattering or effective cross-sectional area, which can affect resistance.

Electromagnetic Interactions. Exponential functions are associated with electromagnetic interactions and fields, which become significant during short circuit events and can contribute to non-linear resistance behavior.

5.5 Model Versatility

The exponential form offers a versatile approach to modeling resistance changes during a short circuit. By adjusting the constants a and b, the form can adapt to different short circuit scenarios, such as variations in conductor material, geometry, and external conditions.

5.6 Implications for Circuit Analysis and Beyond

Beyond rectifying paradoxes, the modified Ohm's Law offers a more accurate framework for circuit analysis, particularly in scenarios involving extremely small resistance values. It accounts for the non-linear behavior of materials, components, and systems, a feature required to enable scientists and engineers to design and predict behavior with greater precision. This newfound accuracy extends to applications involving semiconductor devices, temperature-sensitive elements like thermistors, high-current scenarios, and materials with varying resistivities.

6. CONCLUSİON

The modified Ohm's Law represents a paradigm shift in electrical circuit analysis. By addressing the shortcomings of the standard Ohm's Law and reconciling physics with philosophical principles, this paper introduces a powerful alternative equation. The derived equation not only rectifies the false notion of infinite current at zero resistance but also aligns with our experiential understanding and fundamental philosophical principles. Through rigorous derivation, theoretical examination, and computational analysis, the paper has showcased the accuracy and practicality of the modified Ohm's Law across various scenarios. From semiconductor devices to low-resistance measurements and high-current applications, the equation offers improved accuracy and predictive capabilities. Moreover, this paper bridges the gap between scientific exploration and philosophical principles. It demonstrates the interplay between empirical observations and abstract philosophical concepts, highlighting the importance of interdisciplinary perspectives in advancing our understanding of the universe. The modified Ohm's Law not only enhances our ability to analyze electrical circuits with precision but also invites us to explore the deeper connections between science, philosophy, and mathematics. Embracing this new equation, one embarks on a journey of innovation and discovery, enriching comprehension of both the tangible and the abstract aspects of electrical circuitry.

SIMILARITY RATE: 7%

AUTHOR CONTRIBUTION

First Author: Conceptualization, methodology, data curation, writing, editing etc.

CONFLICT of INTEREST

The authors declared that they have no known conflict of interest.

ACKNOWLEDGEMENT

The author expresses sincere thanks to Daniel Sankei for his invaluable efforts in examining the modified version of Ohm's Law and the scrupulous computational analysis that ensued. Daniel's dedication to examining the theoretical frameworks and computational simulations significantly enhanced the overall quality of the project.

REFERENCES

[1] K. M. Tenny and M. Keenaghan, "Ohms Law," in StatPearls, Treasure Island (FL): StatPearls Publishing, 2023. Accessed: Aug. 31, 2023. [Online]. Available: http://www.ncbi.nlm.nih.gov/books/NBK441875/

[2] D. L. Terrell, "Amplifiers," in Op Amps, Elsevier, 1996, pp. 36–133. doi: 10.1016/B978-075069702-6/50003-2.

[3] W. M. Saslow, "Ohm's Law: Electric Current Is Driven by Emf, and Limited by Electrical Resistance," in Electricity, Magnetism, and Light, Elsevier, 2002, pp. 281–335. doi: 10.1016/B978-012619455-5.50007-3.

[4] R. Mancini, "Review of Circuit Theory," in Op Amps for Everyone, Elsevier, 2009, pp. 7–20. doi: 10.1016/B978-1-85617-505-0.00002-8.

[5] M. Plonus, "Circuit Fundamentals," in Electronics and Communications for Scientists and Engineers, Elsevier, 2020, pp. 1–78. doi: 10.1016/B978-0-12-817008-3.00001-2.

[6] K. Hess, G. Nimtz, and K. Seeger, "Non-ohmic microwave conductivity in semiconductor posts," Solid-State Electron., vol. 12, no. 2, pp. 79–84, Feb. 1969, doi: 10.1016/0038-1101(69)90115-4.

[7] D. Matz and F. Garcia-Moliner, "Non-Ohmic Transport in Semiconductors in a Magnetic Field," Phys. Status Solidi B, vol. 5, no. 3, pp. 495–509, 1964, doi: 10.1002/pssb.19640050306.

[8] W. Shockley, "Hot electrons in germanium and Ohm's law," Bell Syst. Tech. J., vol. 30, no. 4, pp. 990–1034, 1951.

[9] J. Yamashita and K. Inoue, "Hot electron in n-type germanium," J. Phys. Chem. Solids, vol. 12, no. 1, pp. 1–21, Dec. 1959, doi: 10.1016/0022-3697(59)90247-1.

[10] B. Collum, "Electrical," in Nuclear Facilities, Elsevier, 2017, pp. 313–348. doi: 10.1016/B978-0-08-101938-2.00010-6.

[11] P. Heering, J. Keck, and G. A. Rohlfs, "Laboratory Notes, Laboratory Experiences, and Conceptual Analysis: Understanding the Making of Ohm's First Law in Electricity," Berichte Zur Wiss., vol. 43, no. 1, pp. 7–27, 2020, doi: 10.1002/bewi.201900019.

[12] B. Carter, "Review of Op Amp Basics," in Op Amps for Everyone, Elsevier, 2013, pp. 7–17. doi: 10.1016/B978-0-12-391495-8.00002-7.

[13] S. Abdollahi, "Hypothesis of Nothingness," vol. 10, pp. 43–49, Jul. 2021, doi: 10.5923/j.astronomy.20211002.02.

[14] S. Carroll, "Why Is There Something, Rather Than Nothing?," Feb. 2018.

[15] R. L. Anjum and S. Mumford, "A Powerful Theory of Causation," vol. 9780203851289, Jan. 2010, doi: 10.4324/9780203851289.

[16] G. M. D'Ariano, "Causality re-established," Philos. Transact. A Math. Phys. Eng. Sci., vol. 376, no. 2123, p. 20170313, Jul. 2018, doi: 10.1098/rsta.2017.0313.

[17] S. Mumford and R. L. Anjum, "Fundamentals of causality," Inf.-Knowl.-Syst. Manag., vol. 10, pp. 75–84, Jan. 2011, doi: 10.3233/IKS-2012-0186.

[18] M. Lincoln and A. Wasser, "Spontaneous creation of the Universe Ex Nihilo," Phys. Dark Universe, vol. 2, no. 4, pp. 195–199, Dec. 2013, doi: 10.1016/j.dark.2013.11.004.

[19] A. Kimuya, On the Law of Energy Conservation: A Provable Review. 2022. doi: 10.13140/RG.2.2.24660.68482.

[20] G. Chatzarakis, M. Tortoreli, and A. Tziolas, "Thevenin and Norton's Theorems: Powerful Pedagogical Tools for Treating Special Cases of Electric Circuits," Int. J. Electr. Eng. Educ., vol. 40, Oct. 2003, doi: 10.7227/IJEEE.40.4.6.

[21] M. Kojić, M. Milošević, and A. Ziemys, "Fundamental laws for physical fields and mechanics," in Computational Models in Biomedical Engineering, Elsevier, 2023, pp. 21–45. doi: 10.1016/B978-0-323-88472-3.00004-9.

[22] F. Fasmin and R. Srinivasan, "Review—Nonlinear Electrochemical Impedance Spectroscopy," *J. Electrochem. Soc.*, vol. 164, no. 7, p. H443, May 2017, doi: 10.1149/2.0391707jes.

[23] IEEE Industry Applications Society, IEEE-SA Standards Board, and American National Standards Institute, Eds., *IEEE recommended practice for calculating short-circuit currents in industrial and commercial power systems*. New York, N.Y: Institute of Electrical and Electronics Engineers, 2006.

[24] A. Lukichev, "Physical meaning of the stretched exponential Kohlrausch function," *Phys. Lett. A*, vol. 383, no. 24, pp. 2983–2987, Aug. 2019, doi: 10.1016/j.physleta.2019.06.029.

[25] P. Peterson *et al.*, "Practical Use of Metal Oxide Semiconductor Gas Sensors for Measuring Nitrogen Dioxide and Ozone in Urban Environments," *Sensors*, vol. 17, no. 7, p. 1653, Jul. 2017, doi: 10.3390/s17071653.

Appendix I. Parameter x associated practical's factors for the modified Ohm's law

Length of the Conductor ($x = Length$). In the case of the conductor's length being the parameter x, the resistance $R(x)$ can be influenced by the physical dimensions of the conductor. As the conductor length increases, the resistance also increases due to the longer path electrons have to traverse. For instance, during a short circuit, where the length becomes negligible, the resistance $R(x)$ is expected to decrease significantly, allowing for a higher current flow.

Cross-Sectional Area ($x = Area$). The cross-sectional area of the conductor can also play a role. A larger cross-sectional area allows for more electron movement, resulting in lower resistance. In a short circuit, when the conductor is effectively reduced to a point, the cross-sectional area no longer significantly influences resistance, leading to the assumption of very low resistance.

Temperature ($x = Temperature$). Temperature is a critical factor affecting resistance. Higher temperatures can lead to increased resistance due to increased scattering of electrons. In the context of a short circuit, the intense current flow generates heat, potentially causing a rise in temperature. This can further decrease resistance, leading to a self-reinforcing cycle. Considering x as temperature, $R(x)$ can capture this non-linear relationship.

Material Properties ($x = Material\ Prperties$). Different materials have different resistivities. The parameter x could be associated with material properties that influence resistance. For instance, variations in impurities, crystal structure, or electron mobility can lead to different resistance behaviors during a short circuit.

Electromagnetic Interactions ($x = Magnetic\ Field\ Intensity$). In cases where electromagnetic fields are present, the parameter x could represent the intensity of the magnetic field. This can affect the motion of charge carriers and hence resistance. During a short circuit, magnetic interactions could contribute to complex and non-linear resistance changes.

Geometric Configurations ($x = Geometry$). The geometry of the conductor itself, including its shape and orientation, can be linked to x. Changes in geometry can introduce complex interactions between electrons and the conductor's structure, affecting resistance in novel ways during a short circuit.

External Environmental Factors ($x = External\ Factors$). External factors such as pressure, humidity, or radiation could also be associated with x. These factors might induce changes in the conductor's physical properties, affecting resistance behavior during a short circuit event.

Structural Integrity ($x = Structural\ Integrity$). In scenarios where the conductor's structural integrity is compromised, x could represent the extent of damage or deformation. Changes in the conductor's physical structure can influence resistance and its behavior during a short circuit.

In essence, incorporating the parameter x, the modified Ohm's law equation allows us to explore and model a wider range of factors that influence resistance during a short circuit.

Appendix II. Choice of the Exponential Function $R(x) = a \times e^{bx}$

The choice of the exponential function $R(x) = a \times e^{bx}$ as the form of the modified Ohm's Law is motivated by its suitability in capturing the behavior of resistance in scenarios involving extremely low resistance values [22-25]. This specific form was preferred for several reasons including the following.

Empirical Observations. Extensive empirical data and observations from practical electrical circuits and short circuits indicate that resistance often follows an exponential trend when approaching very low values [23]. This is particularly evident in scenarios where metallic conductors or semiconductor devices experience extreme conditions.

Physical Plausibility. The exponential function aligns with the physical plausibility of resistance behavior during short circuits. It reflects the tendency of resistance to impede current flow as it approaches zero, preventing both infinite current and zero resistance, which would be unphysical.

Consistency with Experimental Data. The exponential function $R(x) = a \times e^{bx}$ has been found to provide a good fit for resistance data in numerous experiments involving low-resistance measurements. This consistency supports its choice as a suitable mathematical model for such scenarios.

While the exponential form has been selected as the primary form for the modified Ohm's Law, it is important to note that other exponential functions could also be considered. However, the chosen form offers a robust and coherent representation of resistance behavior and is preferred for its empirical and physical consistency in addressing the limitations of the conventional Ohm's Law.

Eurasian Journal of Science Engineering and Technology

Research Article

INSIGHT INTO ANTI-CORROSION EFFECT OF *MAMMILLARIA PROLIFERA* FRUIT EXTRACT AS A GREEN INHBITOR FOR MILD STEEL IN HCl SOLUTION

Demet ÖZKIR[1,*]

[1,*] *Niğde Ömer Halisdemir University, Faculty of Arts & Sciences, Department of Chemistry, Niğde, 51240, Türkiye*

ABSTRACT

In this study, it was aimed to examine the adsorption and corrosion behaviours of the aqueous extract of *Mammillaria prolifera*, a cactus fruit, in 1.0 M HCl solution using experimental methods such as potentiodynamic polarization and electrochemical impedance spectroscopy (EIS). *Mammillaria prolifera* is a cactus species from the Cactaceae family, commonly known as Texas nipple cactus. Experiments were realized for aqueous extracts of four different *Mammillaria prolifera* fruits. The results indicate that the aqueous extract solution of cactus fruit has outstanding anti-corrosive performance of over 90% at the optimum concentration of 0.120% (w/v). In addition to electrochemical experiments, FE-SEM surface images were taken as another indicator of high inhibition. The results showed that the mild steel surface immersed in the inhibited electrolyte solution at 298 K after one-hour exposure did not contain cracks, pits or deformations compared to the inhibitor-free surface. As a result, experimental measurements and FE-SEMsurface images support each other.

Keywords: *Mammillaria prolifera*, Green inhibitor, Adsorption, Mild steel, EIS.

1. INTRODUCTION

Corrosion, the gradual degradation of materials due to electrochemical reactions with their environment, poses a significant economic and safety challenge across various industries. Mild steel, widely employed as a structural material in various industrial applications, is favored for its combination of durability and workability [1]. However, when subjected to acidic environments, mild steel exhibits a high susceptibility to corrosion. Acidic corrosion poses a critical challenge, often leading to costly damage and functional impairment of steel structures. In industrial processes where acidic environments are prevalent, in energy production facilities, and in numerous sectors where chemical processes occur, mild steel structures are constantly exposed to acidic mediums [2]. This exposure accelerates the formation of rust layers on the steel surface, jeopardizing structural integrity. Therefore, comprehending the fundamental mechanisms of acidic corrosion and developing effective measures is of paramount importance to enhance the durability of soft steel structures and ensure their long-term viability [3].

To mitigate corrosion, numerous approaches have been explored, including the application of protective coatings, alloy modifications, and the use of corrosion inhibitors. The utilization of corrosion inhibitors, in particular, has garnered significant attention for its potential to impede or slow down corrosion processes [4]. This study will delve into the corrosion mechanisms of mild steel in acidic media and meticulously address the plant extract influencing this mechanism. Such environmentally friendly compounds, called green, contain elements in their structures that prevent corrosion and minimize the harmful effects of corrosion, as they contain aromatic rings that can bind and adsorb to the surface of the metal, and heteroatoms with double bonds and/or unpaired electron pairs [5,6].

Plant extracts, owing to their rich phytochemical composition, have emerged as promising candidates for corrosion inhibition. These extracts are abundant sources of secondary metabolites such as alkaloids, flavonoids, tannins, and phenolic compounds, which have demonstrated notable anti-corrosive properties in other laboratory settings [7,8]. The utilization of plant extracts as corrosion inhibitors not only presents an eco-friendly alternative to synthetic chemicals but also taps into the wealth of bioactive compounds that plants have evolved to defend against environmental stresses [9,10]. This paper aims to provide a comprehensive review of the current state of research on the utilization of plant extracts as corrosion inhibitors. By examining the inhibitory mechanisms and effectiveness of various plant-derived compounds, it was sook to contribute to the growing body of knowledge in corrosion science and offer insights into the potential practical applications of botanical extracts in corrosion control strategies.

Mammillaria prolifera, commonly known as the Texas Nipple cactus, is a species of cactus grown as an ornamental plant. While *Mammillaria prolifera* is primarily known for its distinctive cylindrical or globular shape and its ability to produce offsets (small new plants) prolifically, it is not typically cultivated for its fruit. However, like many cactus species, *Mammillaria prolifera* does produce small, fleshy fruits after flowering. These fruits are typically small, round, and may range in color from

* Corresponding author, e-mail: dozkir@ohu.edu.tr (D. Özkır)
Recieved: 07.11.2023 Accepted: 06.12.2023
doi: 10.55696/ejset.1387199

green to reddish, depending on the species and the degree of ripeness. The fruits of *Mammillaria prolifera*, like those of many cacti, are not typically consumed by humans and are not considered a significant part of the human diet [11].

In the light of this idea, in this study, the effect of *Mammillaria prolifera* fruit aqueous extract from the cactus species as an environmentally friendly green inhibitor on the corrosion of mild steel electrodes kept in 1.0 M HCl solution for one hour was investigated by two electrochemical methods. This study is also noteworthy because there is no previous study in the literature showing that this fruit extract of cactus species has been used as an inhibitor to inhibit metallic corrosion.

2. MATERIAL AND METHOD

2.1. The extract solutions of *Mammillaria prolifera* fruits

Mammillaria prolifera fruit, which was weighed about 10 g (Figure 1), was put into a 250 mL reaction flask and refluxed for 16 hours by adding enough distilled water. After 16 h of reflux process, the extract was filtered and its volume was approximately 120 mL. Its colour is light yellow. The concentration of the stock *M. prolifera* solution studied was calculated as 0.240% (w/v). Other concentrations were diluted from the stock solution. Following the preparation of the stock solution, the concentrations utilized for electrochemical experiments ranged from the highest concentration at 0.120% (w/v) to the lowest at 0.015% (w/v). These concentrations were established as 0.120% (w/v), 0.060% (w/v), 0.030% (w/v), and 0.015% (w/v), respectively, in order of decreasing strength. In Figure 2, a stereo-microscope image of the cactus fruit at a scale of 1000 μm is shown to make the study more understandable. Conducting experiments in a 1.0 M HCl (hydrochloric acid) solution allows for the study of electrochemical behaviour in an acidic medium.

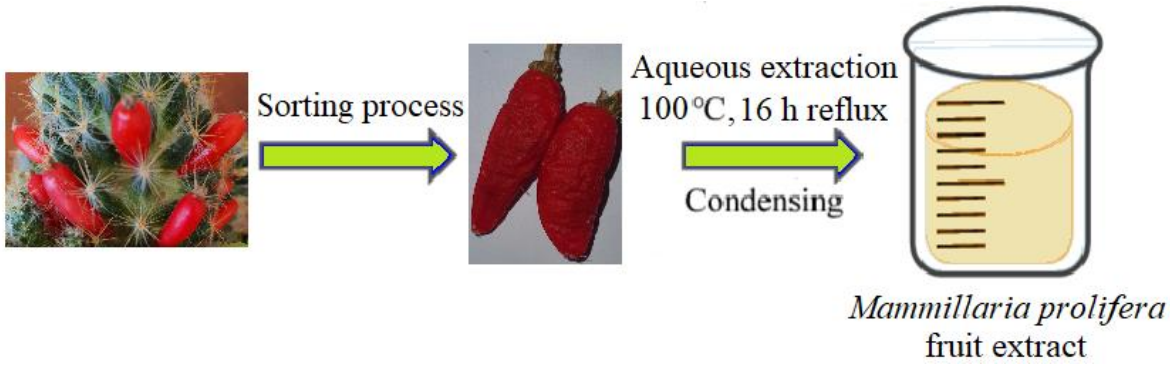

Figure 1. Schematic diagram for the preparation process of *M. prolifera* fruit extract.

Figure 2. Stereo microscope image of *M. prolifera* fruit.

2.2. Electrodes and electrochemical methods

The working electrode consisted of mild steel with the following weight percentage composition: 0.01100% P, 0.06030% Cr, 0.08400% C, 0.07890% Ni, 0.00222% Nb, 0.01100% V, 0.21700% Cu, 0.01040% Mo, 0.01900% S, 0.40900% Mn, 0.10200% Si, 0.01620% Sn, 0.00198% Co, and 98.977% Fe. These electrodes were inserted into a cylindrical mold containing polyester, exposing an area of 0.5024 cm^2 to the aggressive solution. The test electrodes were meticulously polished using abrasive paper with 150 and 600 grits. Subsequently, the electrode surfaces were thoroughly cleaned with acetone and distilled water. For electrochemical experiments, a three-electrode system was employed. The first electrode utilized was the mild steel working electrode. The latter electrode, serving as the counter electrode, consisted of a platinum plate with a surface area of 2.0 cm^2. The last electrode utilized was Ag/AgCl (3.0 M KCl), employed as the reference electrode. All potentials recorded in this study are referenced to the Ag/AgCl electrode.

Utilizing a computer-controlled CHI 660B model electrochemical analyser, electrochemical impedance spectroscopy (EIS) and potentiodynamic polarization tests were executed. These assessments were carried out in a 1.0 M HCl solution with and without four concentrations of *M. prolifera* fruit extract. Prior to commencing all electrochemical tests, the working electrodes were immersed in the working solution for one hour to ensure stabilization of the open circuit potential (E_{corr}) at 298 K. EIS experiments were conducted at the E_{corr}, encompassing a frequency range from 10^5 to $5x10^{-3}$ Hz, with a 5 mV amplitude applied to the system. The potentiodynamic polarization tests were registered at cathodic/anodic potentials of ±0.350 V relative to E_{corr}, respectively. This was performed at a scan rate of 1.0 mV s^{-1}. Surface analysis images were captured over the course of one hour in an aggressive solution (blank) both with and without *M. prolifera* fruit extract, employing the FE-SEM technique (Zeiss GeminiSEM 500 with computer control).

3. RESULTS AND DISCUSSION

3.1. Electrochemical measurement findings

It is crucial that the chosen method for corrosion rate assessment minimally alters the innate structure of the metal surface. Hence, alternative current impedance, an electrochemical technique believed to exert minimal influence on the metal's nature, stands out as one of the most favoured approaches [12]. The inhibitory impact of *M. prolifera* fruit extract on the mild steel surface, exhibiting a green inhibitory effect, was assessed through EIS and potentiodynamic polarization methods during a one-hour immersion period at 298 K across four various concentrations. In this procedure, two sets of electrical equivalent circuit models were employed; Figure 3 for 1.0 M HCl and Figure 4 for the inhibited solutions. The corrosion and inhibition processes' equivalent circuits were derived from the EIS data with the aid of Zview2 software.

In Figures 3 and 4, it is evident that the two proposed circuits exhibit notable distinctions. Notably, for solutions containing *M. prolifera* fruit extract, a distinct inhibitor film forms on the mild steel surface, resulting in a corresponding increase in resistance. Figure 4 provides a clearer insight, illustrating that the addition of *M. prolifera* fruit extract in varying concentrations to the 1.0 M HCl solution leads to a reduction in mild steel electrode corrosion. This occurs as the *M. prolifera* fruit extract adsorbs onto the mild steel surface, creating a protective film layer that effectively hinders corrosion. Additionally, the EIS diagram in Figure 4 vividly portrays the increased diameters of the capacitive loops in direct correlation to the rise in *M. prolifera* fruit extract concentration.

The pertinent EIS and potentiodynamic polarization parameters have been summarized in Table 1. The impedance plots are characterized by two distinct frequency regions: the high frequency region pertains to the diffuse layer (R_d) and charge transfer (R_{ct}) in the corrosion process. The low frequency region is where inhibition occurs, governed by the film resistance (R_f) that forms on the mild steel surface, originating from the *M. prolifera* fruit extract. Additionally, two constant phase elements (*CPE*) are present in the cactus fruit extract solution process. The first represents the double layer capacitance (CPE_{dl}), while the second corresponds to the capacitance of the film layer on the mild steel (CPE_{film}). Upon examination of the polarization resistance values derived from the EIS measurements in Table 1, it was evident that the inhibition efficiency values ($\eta\%$) increased with the addition of the extract of cactus fruit to the aggressive solution. The inhibition efficiency values calculated from the results of the EIS method ranged from 88.6% to 91.4%. The capacitance value (CPE) in the blank solution measured at 110 $\mu F/cm^2$. However, it was observed that this value significantly increased when M. prolifera fruit extract was introduced into the HCl solution. The range of CPE values varied between 82–51 $\mu F/cm^2$. Additionally, the corrosion potential value (E_{corr}), initially at -0.474 V in the HCl electrolyte, shifted towards more cathodic potentials in solutions containing cactus fruit extract (refer to Table 1).

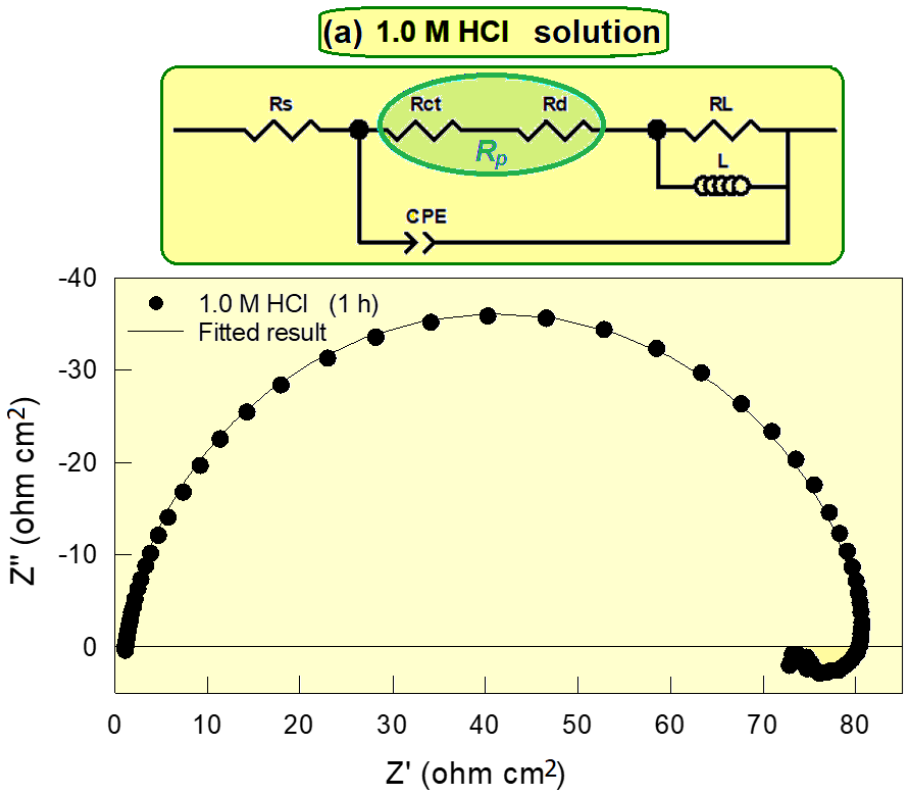

Figure 3. Electrical equivalent circuit proposed and EIS diagram for 1.0 M HCl solution after 1 h immersion.

The dissolution treatment parameters of the mild steel electrode, determined using the Tafel extrapolation method - an alternative electrochemical technique, are presented in Table 1.

Table 1. EIS and potentiodynamic polarization findings determined from the tests in solutions without and with *M. prolifera* fruit extract

***C* (w/v %)**	**EIS**							
***Mammillaria prolifera* fruit extract**	E_{corr} **(V/Ag/AgCl)**	R_s **(Ω cm^2)**	***CPE***		R_L **(Ω cm^2)**	***L* (*H*)**	R_p **(Ω cm^2)**	η **(%)**
			($\mu F\ cm^{-2}$)	***n***				
1.0 M HCl	-0.474	1.2	110	0.94	8	4	72	-
0.015	-0.525	1.1	82	0.74	-	-	630	**88.6**
0.030	-0.531	1.2	71	0.70	-	-	700	**89.7**
0.060	-0.523	1.0	60	0.67	-	-	780	**90.8**
0.120	-0.522	1.3	51	0.65	-	-	840	**91.4**

***Mammillaria prolifera* fruit extract**	***Potentiodynamic polarization**			
	$^*E_{corr}$ **(V/Ag/AgCl)**	$-\beta_c$ **($mV\ dec^{-1}$)**	i_{corr} **($\mu A\ cm^{-2}$)**	$^*\eta$ **(%)**
1.0 M HCl	-0.475	108	265	-
0.015	-0.526	102	33	**87.5**
0.030	-0.535	104	29	**89.1**
0.060	-0.525	100	25	**90.6**
0.120	-0.524	98	23	**91.3**

INSIGHT INTO ANTI-CORROSION EFFECT OF MAMMILLARIA PROLIFERA FRUIT EXTRACT AS A GREEN INHBITOR FOR MILD STEEL IN HCl SOLUTION

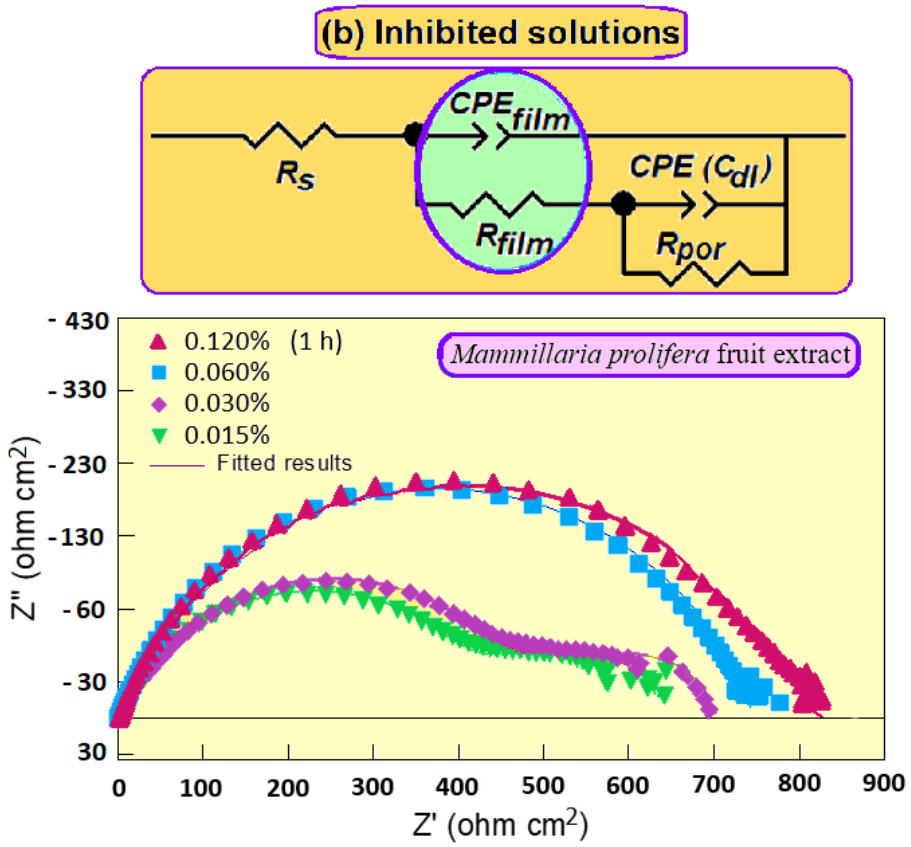

Figure 4. Electrical equivalent circuit proposed and EIS diagrams in containing different concentrations of *M. prolifera* fruit extract.

Figure 5 provides the potentiodynamic polarization plots for the working electrodes in HCl solution at 298 K, with four varying concentrations of *M. prolifera* fruit extract. In the absence of the extract, the corrosion current density (i_{corr}) measured 265 µA/cm². However, with the introduction of the cactus fruit extract into the HCl solution, these values gradually decreased.

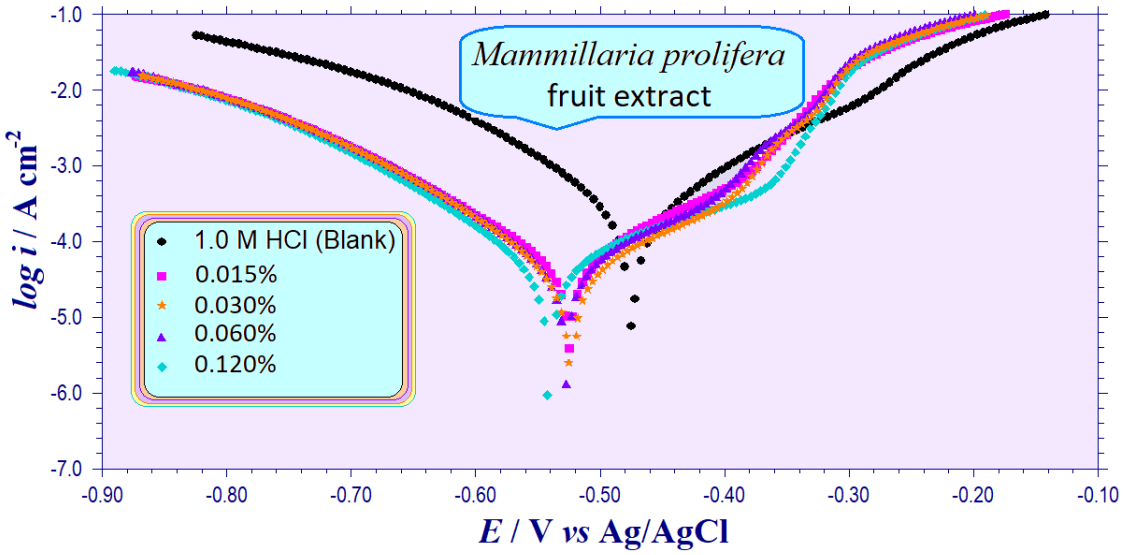

Figure 5. Potentiodynamic polarization plots of mild steels in HCl solution for four concentrations of *M. prolifera* fruit extract.

In all experimental solutions, as the concentration of *M. prolifera* fruit extract increased, corrosion current density (i_{corr}) values decreased, and inhibition efficiency values rose. While the cathodic Tafel constant ($-\beta_c$) was 108 *mV/dec* in the blank solution, it varied between 98 *mV/dec* and 104 *mV/dec* in the solutions with the inhibitor. The relatively stable cathodic Tafel constants across solutions with and without M. prolifera fruit extract suggest that the mechanism of hydrogen formation remained largely unaffected by the studied inhibitor. The semi-logarithmic current-potential curves and Table 1 collectively demonstrate that the ${}^{*}E_{corr}$ values, calculated by Tafel extrapolation of cathodic and anodic curves for the mild steel electrode at 298 K in an uninhibited solution, were recorded at -0.475 V. However, with the introduction of *M. prolifera* fruit extract solutions, the ${}^{*}E_{corr}$ values shifted towards more cathodic potentials.

Upon examining the cathodic plots depicted in Figure 5, it is evident that the addition of *M. prolifera* fruit extract led to a substantial reduction in current density within the 1.0 M HCl solution. This observation suggests that the *M. prolifera* fruit extract acted as a cathodic inhibitor in the 1.0 M HCl solution [13]. The findings obtained from both experimental methods complemented each other, leading to the conclusion that the adsorption of M. prolifera fruit extract on the metal surface is an inevitable phenomenon. Moreover, this extract can be considered a green inhibitor, as it does not have any adverse environmental effects.

3.2. Surface analysis by FE-SEM

Given that FE-SEM stands for field emission scanning electron microscope, it offers the capability to conduct surface analysis with significantly higher resolution, resulting in much clearer images [14]. Comprehensive surface analyses were conducted through FE-SEM analysis to elucidate the surface morphologies of mild steel electrodes that were immersed in 1.0 M HCl solutions, both with and without *M. prolifera* fruit extract at the highest concentration (0.120% w/v), at a constant temperature of 298 K for one hour. The FE-SEM morphologies are presented in Figure 6.

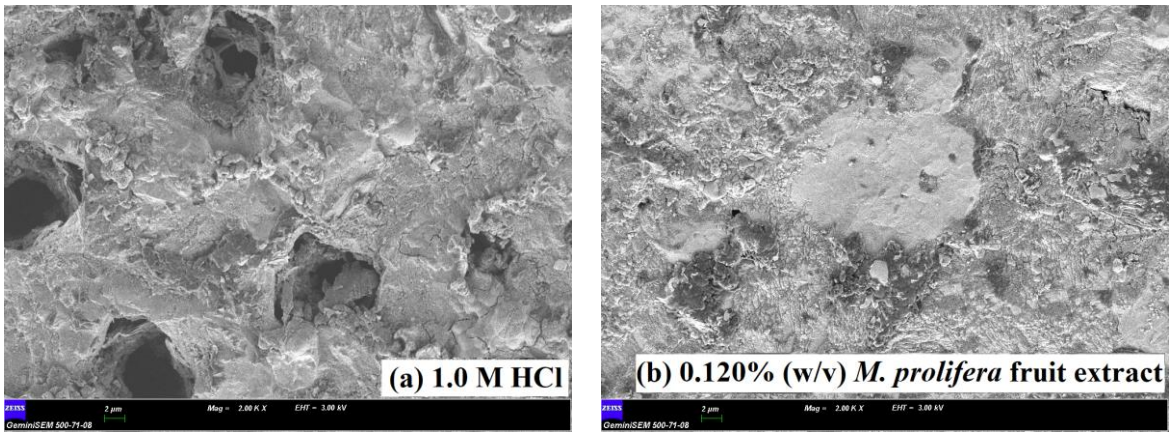

Figure 6. FE-SEM surfaces of the mild steels for 1 h exposure.

It was noted that the surface of the metal immersed in the solution without the inhibitor exhibited indentations and pit-like appearances. Conversely, the electrode immersed in the solution containing *M. prolifera* fruit extract appeared flatter, with a reduction in both the number and size of pits.

4. CONCLUSION

This study holds significance in first utilizing *M. prolifera* fruit extract from the Cactaceae family as an environmentally friendly and green inhibitor for mild steel in HCl solution. Through 1-hour exposure tests conducted by two different methods, it was observed that the M. prolifera fruit extract exhibited strong adsorption onto the mild steel surface, resulting in an inhibition rate of over 90% at its optimal concentration. The chemical composition of phytochemicals (secondary metabolites) present in M. prolifera fruit, characterized by aromatic rings, double bonds between phenolic groups, flavonoids, terpenoids, among others, plays a pivotal role in achieving such high inhibition efficiency against mild steel corrosion. This inhibitor effect, stemming from naturally derived, eco-friendly compounds, holds paramount importance for both industrial processes and the environment, given their biodegradable nature and absence of toxic components. The results obtained by the experimental method are quite consistent with the surface findings.

INSIGHT INTO ANTI-CORROSION EFFECT OF MAMMILLARIA PROLIFERA FRUIT EXTRACT AS A GREEN INHBITOR FOR MILD STEEL IN HCl SOLUTION

SIMILARITY RATE: 20%

AUTHOR CONTRIBUTION

Demet Özkır: Conceptualization, methodology, data curation, writing, editing etc.

CONFLICT of INTEREST

The author declares no conflict of interest.

ACKNOWLEDGEMENT

The author would like to thank to Prof. Dr. Osman Seyyar for photographed in his laboratory of the *M. prolifera* fruit material.

REFERENCES

[1] H. Kahkesh, B. Zargar, "Estimating the anti-corrosive potency of 3-nitrophthalic acid as a novel and natural organic inhibitor on corrosion monitoring of mild steel in 1 M HCl solution*," Inorganic Chemistry Communications*, vol. 158, Oct., pp. 111533, 2023.

[2] Y. Li, Z. Li, T. Ma, L. Zeng, H. Chen, X. Lei, K. Ma, Z. Zhang, Y. Ding, J. Han, "Corrosion mitigation of peanut shell extract as a novel effective corrosion inhibitor for carbon steel in sulfuric acid medium," *Journal of Materials Research and Technology*, 2023 (Article in Press). doi: https://doi.org/10.1016/ j.jmrt.2023.10.212.

[3] M. Chafiq, A. Chaouiki, M. R. Albayati, H. Lgaz, R. Salghi, S. K. AbdelRaheem, I. H. Ali, S. K. Mohamed, I-M. Chung, "Unveiled understanding on corrosion inhibition mechanisms of hydrazone derivatives based on naproxen for mild steel in HCl: A joint experimental/theoretical study," *J. Mol. Liq.*, vol. 320, 2020.

[4] M. Abdallah, H. Al-Tass, B.A. Jahdaly, A. Fouda, "Inhibition properties and adsorption behavior of 5-arylazothiazole derivatives on 1018 carbon steel in 0.5 M H2SO4 solution," *J. Mol. Liq.*, vol. 216, pp. 590–597, 2016.

[5] A. Fouda, S. Abd El-Maksoud, A. El-Hossiany, A. Ibrahim, "Corrosion protection of stainless steel 201 in acidic media using novel hydrazine derivatives as corrosion inhibitors," *Int. J. Electrochem. Sci.*, vol. 14, pp. 2187–2207, 2019.

[6] M. Talebian, K. Raeissi, M. Atapour, B. Fern´andez-P´erez, A. Betancor-Abreu, I. Llorente, S. Fajardo, Z. Salarvand, S. Meghdadi, M. Amirnasr, "Pitting corrosion inhibition of 304 stainless steel in NaCl solution by three newly synthesized carboxylic Schiff bases," *Corros. Sci.*, vol. 160, pp. 108130, 2019.

[7] S. H. Alrefaee, K. Y. Rhee, C. Verma, M. A. Quraishi, E. E. Ebenso, "Challenges and advantages of using plant extract as inhibitors in modern corrosion inhibition systems: Recent advancements," *J. Mol. Liq.*, vol. 321, 2021.

[8] N. D. Gowraraju, S. Jagadeesan, K. Ayyasamy, L. O. Olasunkanmi, E. E. Ebenso, C. Subramanian, "Adsorption characteristics of Iota-carrageenan and Inulin biopolymers as potential corrosion inhibitors at mild steel/sulphuric acid interface," *J. Mol. Liq.*, vol. 232, pp. 9-19, 2017.

[9] D. Özkır, "An Overview of *Plagiochila porelloides* (Marchantiophyta) as a New Environmentally Sustainable Green Corrosion Inhibitor for Mild Steel in Acidic Solution," *Anatolian Bryol.*, vol. 7, no. 2, pp. 119-130, 2021.

[10] D. Özkır, "The Green Inhibitive Effect of *Ptychostomum schleicheri* (Bryophyta) Extract on Mild Steel Corrosion," *Anatolian Bryology*, vol. 8, no. 2, pp. 114-122, 2022.

[11] [Online]. Available: https://www.gardenia.net/plant/mammillaria-prolifera#:~:text=They%20give%20way%20to%20edible,outdoors%20in%20frost-free%20climates. [Accessed: Nov. 1, 2023].

[12] M. Erbil, "Korozyon İlkeler – Yöntemler," *Korozyon Derneği Yayını*, Poyraz Ofset, Ankara, 2012.

[13] S. Akkoç, D. Özkır, E. Başaran, S. Kaya, A. Berisha, "A combined experimental and theoretical approach effect of a benzimidazolium salt as a new corrosion inhibitor on mild steel in HCl solution," *Ionics*, vol. 29, pp. 3813–3827, 2023.

[14] D. K. Singh, E. E. Ebenso, M. K. Singh, D. Behera, G. Udayabhanu, R. P. John, "Non-toxic Schiff bases as efficient corrosion inhibitors for mild steel in 1 M HCl: Electrochemical, AFM, FE-SEM and theoretical studies," *Journal of Molecular Liquids*, vol. 250, pp. 88–99, 2018.